Journal of Hydrology

3D numerical modelling of flow exchanges between flooded streets and residential blocks during urban flooding in an idealized district

--Manuscript Draft--

Manuscript Number:	HYDROL63307R1
Article Type:	Research paper
Keywords:	Urban Flooding; Flow structure; Turbulence model; 3D numerical modelling; Reynolds-averaged Navier-Stokes equations
Corresponding Author:	Lihua Chen, Ph.D. Guangxi University Nanning, CHINA
First Author:	Xuefang Li
Order of Authors:	Xuefang Li
	Shuyue Yu
	Vasileios Kitsikoudis
	Guilhem Dellinger
	Lihua Chen, Ph.D.
	Sébastien Erpicum
	Léo Guiot
	Chengguang Lai
	Benjamin Dewals
Abstract:	Flow exchanges between flooded streets and the interior of buildings through broken doors and windows can have a significant impact on the flow characteristics and the flood hazard in urban floods. Traditionally, urban floods are modelled with 2D shallow-water equations, however, this modelling approach is not always capable to reproduce such complicated flow exchanges. This study aims to investigate the added value of 3D non-hydrostatic numerical modelling over the modelling with 2D shallow-water equations for the accurate prediction of flow exchanges between flooded streets and the interior of buildings. Systematic comparisons were carried out between the results of 2D depth-averaged and 3D numerical modelling against laboratory observations for eight configurations of an urban block surrounded by flooded streets. Each urban block configuration had a different number and locations of openings in the block perimeter. The 3D model predicted the flow discharge partition at the street outlets more accurately than the 2D model, with an average RMSE of about 1 percentage point compared to the measurements. The flow in the interior of the urban block was typically characterized by large recirculation zones, which were successfully reproduced by the 3D model in terms of number, locations and directionality of recirculating flow, with only limited discrepancies in the sizes and shapes for some cases. The superiority of the 3D model over the 2D was particularly evident in the case where the streets meet a large open space. In addition, 3D models perform better than 2D models in cases with high vertical velocities. The vertical velocities are prominent in areas where flow jets and flow contractions are observed near the openings of the urban blocks, and can reach values up to 20% of the total depth-averaged velocities. The vertical variation of the flow pattern is rather limited from the bottom to the surface, but the difference between the magnitude of the surface velocity and the corresponding depth-averaged velocity reaches 50% in areas of complex flow patterns near the openings of the urban block. From an engineering perspective, this study informs practitioners when to opt for the more demanding 3D modelling instead of the traditional modelling with 2D shallow-water equations in the context of flow exchanges between flooded streets and the interior of buildings during urban floods.
Response to Reviewers:	

3D numerical modelling of flow exchanges between flooded streets and residential blocks during urban flooding in an idealized district

Xuefang Li[(1)], Shuyue Yu[(1)], Vasileios Kitsikoudis[(2)], Guilhem Dellinger[(3)], Lihua Chen[(1)*], Sébastien Erpicum[(4)], Léo Guiot [(3)]; Chengguang Lai[(1,5)], Benjamin Dewals[(4)]

[(1)] College of Civil Engineering and Architecture, Guangxi University, Nanning, China

[(2)] Water Engineering and Management, University of Twente, Enschede, The Netherlands

[(3)] ICube laboratory, National School for Water and Environmental Engineering, Strasbourg, France

[(4)] Hydraulics in Environmental and Civil Engineering (HECE), University of Liège (ULiège), Belgium

[(5)] State Key Laboratory of Subtropical Building and Urban Science, South China University of Technology, Guangzhou, China

*Corresponding authors: Lihua Chen (xdslclh@gxu.edu.cn)

ABSTRACT

Flow exchanges between flooded streets and the interior of buildings through broken doors and windows can have a significant impact on the flow characteristics and the flood hazard in urban floods. Traditionally, urban floods are modelled with 2D shallow-water equations, however, this modelling approach is not always capable to reproduce such complicated flow exchanges. This study aims to investigate the added value of 3D non-hydrostatic numerical modelling over the modelling with 2D shallow-water equations for the accurate prediction of flow exchanges between flooded streets and the interior of buildings. Systematic comparisons were carried out between the results of 2D depth-averaged and 3D numerical modelling against laboratory observations for eight configurations of an urban block surrounded by flooded streets. Each urban block configuration had a different number and locations of openings in the block

perimeter. The 3D model predicted the flow discharge partition at the street outlets more accurately than the 2D model, with an average RMSE of about 1 percentage point compared to the measurements. The flow in the interior of the urban block was typically characterized by large recirculation zones, which were successfully reproduced by the 3D model in terms of number, locations and directionality of recirculating flow, with only limited discrepancies in the sizes and shapes for some cases. The superiority of the 3D model over the 2D was particularly evident in the case where the streets meet a large open space. In addition, 3D models perform better than 2D models in cases with high vertical velocities. The vertical velocities are prominent in areas where flow jets and flow contractions are observed near the openings of the urban blocks, and can reach values up to 20% of the total depth-averaged velocities. The vertical variation of the flow pattern is rather limited from the bottom to the surface, but the difference between the magnitude of the surface velocity and the corresponding depth-averaged velocity reaches 50% in areas of complex flow patterns near the openings of the urban block. From an engineering perspective, this study informs practitioners when to opt for the more demanding 3D modelling instead of the traditional modelling with 2D shallow-water equations in the context of flow exchanges between flooded streets and the interior of buildings during urban floods.

Keywords: Urban flooding; Flow structure; Turbulence model; 3D numerical modelling; Reynolds-averaged Navier-Stokes equations

1 Introduction

The frequency and intensity of extreme urban flooding keep growing given the rapid urbanization observed globally (Chen et al., 2015) and the more frequent extreme rainfall events due to climate change (Deng et al., 2024; Fang, 2016; Hettiarachchi et al., 2018). Considering that such urban flooding events can cause huge economic losses and a high number of fatalities (Kreibich et al., 2019; Li et al., 2020; Mu et al., 2024; UN Office for Disaster Risk Reduction, 2020), flood risk prediction and management become a priority of urban management (Guo et al., 2021; Liao et al., 2023; Luo et al., 2022; Rosenzweig et al., 2021; Yang et al., 2018).

Predicting the dynamics of urban flooding is a major challenge due to the high variability of flow patterns caused by complex urban layouts (Mignot et al., 2022), and multiple features interacting with the flow (e.g., sewer system, buildings, underground spaces, parked vehicles, street furniture) (Chen et al., 2024; Li et al., 2021; Mejía-Morales et al., 2021; Mignot et al., 2019). Meanwhile, flood hazard needs to be assessed by means of flow characteristics, like flow depth, flow velocity, and flood duration, at local scales (Lai et al., 2024; Mejía-Morales et al., 2021; Xia et al., 2014; Zhu et al., 2023). Therefore, advancing the understanding of urban flow processes and accurately quantifying them is of utmost importance (Dewals et al., 2023; Lai et al., 2024; Li et al., 2021).

1.1 Complex flow patterns in urban areas

Recent reviews of experimental and numerical modelling of urban flooding by Luo et al. (2022), Mignot et al. (2022) and Mignot et al. (2019), showed that studies focusing on detailed flow characteristics in urban areas have mostly been conducted for either a single crossroad (Luo et al., 2018; Mignot et al., 2013; Momplot et al., 2017; Schindfessel et al., 2015; Weber et al., 2001), regular arrangements of buildings (Li et al., 2022; Velickovic et al., 2017; Zhou et al., 2016; Zhu et al., 2023), parts of highly idealized districts (Bruwier et al., 2020; Dewals et al., 2023; Finaud-Guyot et al., 2019; Li et al., 2021; Mejía-Morales et al., 2023; Mejía-Morales et al., 2021; Sturm et al., 2018), or, more recently, for flow exchanges between flooded streets and the interior of buildings through doors and windows that were opened or broken during a flood (Paquier et al., 2022). Table 1 categorizes and summarizes key aspects of these studies.

The assumptions underpinning 2D hydrodynamic approximations become questionable when vertical flow accelerations are significant (Rong et al., 2020). This potentially induces three-dimensional flow features, including oblique jumps, complex waves, reflections and recirculation zones (El Kadi Abderrezzak et al., 2011), imposing additional challenges to predict urban surface flows. There have been a few studies have contributed insights into urban flow vertical structures based on 3D velocities when measured in laboratory experiments or simulated with 3D computational models (Luo et al., 2018; Mignot et al., 2012; Schindfessel

et al., 2015; Weber et al., 2001; Zhu et al., 2023). Based on an experimental model of a street network, involving 64 impermeable blocks, Finaud-Guyot et al. (2019) measured more than 1000 vertical velocity profiles, shedding light on the non-uniformity of flow velocity distribution over the flow depth, which may render the 2D depth-averaged approximations insufficient. Luo et al. (2022) highlighted the need to develop 3D models to capture vertical flow features, including vertical turbulence, vortexes, or spiral flows, which are likely to occur in extreme urban flooding. Experimental observations of velocity profiles in a junction by Weber et al. (2001) have been widely used to validate computational models (Chen et al., 2017; Luo et al., 2018), Mignot et al. (2012) conducted experiments to analyze the influence of the tributary flow in a junction on flow structures, and validate a 3D numerical model. Schindfessel et al. (2015) used an ADV to measure vertical velocity profiles in a junction with a chamfered cross-section. They found vertical helicoidal cells along with upwelling flow downstream of the flow junction. Flow secondary currents were also observed and modelled by Ramamurthy et al. (2007) with LDA (Laser Doppler Anemometer) and the 3D RANS (Reynolds-Averaged Navier-Stokes) equations for turbulent unsteady flow. Similar effects were presented in the experiments of Momplot et al. (2017), which revealed a helix-shaped vertical recirculation downstream of the side branch of a three-branch bifurcation model .

In Li et al. (2021), similarities between 2D computed depth-averaged flow velocities and measured surface velocities in a street network were observed for five urban configurations. Nevertheless, some major discrepancies were observed between computations and observations downstream of contraction zones, as well as in configurations with a relatively large open area where the shape of the flow jets were not well predicted by the 2D numerical model. These differences hint at a limitation of the 2D numerical model. Recently, Li et al. (2024) conducted 3D modelling of a part of an urban district of Li et al. (2021), and they captured generally well the trajectory and velocity distribution of surface flow jets and recirculations. This raises the question of identifying in which configurations of urban flooding the 2D depth-averaged approach should better be replaced by a more detailed 3D modelling approach to properly

capture the influence of three-dimensional flow features on flood characteristics. While such a comparison has been done for several different urban settings, as explained in this literature review, the trade-off between fast but potentially inaccurate 2D models and more accurate but slow 3D models has not been explored for the case where there are flow exchanges between flooded streets and the interior of buildings. Mejía-Morales et al. (2021) showed that such flow exchanges can generate complicated flow patterns that alter substantially the flood hazard. Considering that urban floods can develop rapidly, it is of utmost importance for urban flood assessment and management to understand in which cases the added complexity introduced by the flow intrusion into buildings can be properly modelled with 2D numerical models, and in which cases more demanding 3D numerical models should be preferred.

Table 1 Previous experimental and numerical research on detailed flow characteristics during urban flooding.

Reference	**Lab**	**Num 2D**	**Num 3D**	**Modelled configurations**	**Urban details**	**Studied variables**	**Vertical flow structure**
Weber et al. (2001)	√			Junction	NO	Flow depth + Surface velocity + Vertical velocity	Yes
Luo et al. (2018)			√	Junction	NO	Flow depth + Surface velocity + Vertical velocity	Yes
Schindfessel et al. (2015)	√		√	Junction	NO	Vertical flow secondary currents	Yes
Ramamurthy et al. (2007)	√		√	Bifurcation	NO	Flow depth + Vertical velocity	Yes
Momplot et al. (2017)	√		√	Bifurcation	NO	Flow depth + Surface velocity + Vertical velocity	Yes
Mignot et al. (2013)	√		√	Bifurcation	Locations of urban block	Flow depth + surface velocity	No
Dong et al. (2021)	√	√		One street	Building density	Flow depth	No
Rubinato et al. (2022)	√			One street	Manhole	Flow depth	No
Velickovic et al. (2017)	√	√		Grid of building blocks	Various layouts of building block	Flow depth + Computed surface velocity	No
Arrault et al. (2016)	√	√		Grid of building blocks	Street network	Flow depth+ Discharge partition	No
Zhou (2016)	√			Grid of building blocks	Porous building facade	Flow depth + 2D surface velocity	No
Finaud-Guyot et al. (2018)	√			Grid of building blocks	Street widths and angles	Flow depth + Surface velocity	No

Reference	Lab	Num 2D	Num 3D	Modelled configurations	Urban details	Studied variables	Vertical flow structure
Zhu et al. (2023)	√		√	Grid of building blocks	Various layouts of building block	Flow depth + horizontal flow velocity	No
Güney et al. (2014)	√			District	Locations of urban block	Flow depth + Vertical velocity	Yes
Smith et al. (2016)	√	√		District	Locations of urban block	Flow depth + Surface velocity	No
Li et al. (2021)	√	√		District	Various layouts of urban building	Flow depth + Surface velocity + Discharge partition	No
Finaud-Guyot et al. (2019)	√			District	Street network	Flow depth + vertical surface velocity +discharge partition	No
Bruwier et al. (2020)		√		District	Various layouts of urban building	Flow depth + Surface velocity	No
Mejía-Morales et al. (2021)	√			District	Porous building facade	Flow depth + Surface velocity + Discharge partition	No
Paquier et al. (2022)	√	√		One street	Locations of obstacles	Flow depth + Surface velocity + Discharge partition	No
Mejía-Morales et al. (2023)	√			District	Urban storage capacity	Flow depth + Surface velocity + Discharge partition	No
Dewals et al. (2023)	√	√		District	Porous building facade + urban storage capacity	Flow depth + Surface velocity + Discharge partition	No
Li et al. (2024)	√	√	√	District	Channelized street networks	Flow depth + Surface velocity + Discharge partition	Yes
Current study	√	√	√	District	Porous building facade + large open spaces	Flow depth + Surface velocity + Discharge partition + Vertical flow structure	Yes

1.2 Objective of this study

This study aims to investigate the added value of 3D non-hydrostatic numerical modelling over the 2D shallow water equations to accurately predict urban flow patterns and structures in a part of a street network where flow exchanges occur between the flooded streets and the interior of an urban block through openings such as doors that may have opened or broken during the flood. This study complements the 2D modelling study of Dewals et al. (2023) by conducting 3D flow computations for eight representative configurations taken from the experimental data of Mejía Morales (2022).

2 Methodology

2.1 Experimental setup

The 3D simulations conducted in this study are compared against experimental observations produced by Mejía-Morales et al. (2022) and the 2D modelling results from Dewals et al. (2023). Only a brief description of these experiments is summarised in this section. Mejía-Morales et al. (2021) provide a more detailed description.

2.1.1 Model Geometry

The experimental model represents an idealized rectangular urban block surrounded by four streets as depicted in Figure 1. The urban block has openings (see Figure S1 and Table S1 for opening coordinates) in its perimeter that allow flow exchanges between the flooded streets and the empty interior of the block. This enables simulating flow exchanges occurring through openings, such as doors or gates, that open or break during a flood event. Mejía Morales (2022) present 13 different cases, of which eight are simulated in this study and described in Section 2.2. The streets comprise two pairs of parallel roads: the "Left" and "Right" streets, each with a length of 5.4 meters along the *x*-axis, and the "Upstream" and "Downstream" streets, each with a length of 3.2 meters along the *y*-axis. All streets have a uniform rectangular cross-section with a width of 0.15 m. The *x*-direction has a slope of 0.12%, while the *y*-direction is horizontal. The model was constructed with PVC material for the bed and plastic for the sidewalls. The dimensions of the central urban block are 0.96 m × 1.56 m and the walls of the urban block have a thickness of 2 cm and a height of 15 cm. The openings have a rectangular shape with a width of 6 cm and a height that is always higher than the water level.

2.1.2 Hydraulic boundary conditions

In the experimental model, two inlets, Inlet 1 and Inlet 2, were positioned at the upstream end of the Left and Right streets, respectively. Precise regulation of the flow was accomplished with the aid of valve-flowmeter systems for each inlet. Inlet 1 was configured to maintain a consistent flow rate of 4.5×10^{-3} m^3/s, while the flow rate of Inlet 2 was set at 2×10^{-3} m^3/s. The experimental setup also included four outlets at the downstream ends of the four streets, with vertical weirs regulating the flow depth. Among these outlets, Outlet 1 had a weir 4 cm in

height, whereas the remaining three outlets were equipped with weirs 3 cm in height.

2.1.3 Scaling proportions

A geometrically distorted scale was applied, incorporating horizontal and vertical scaling factors of λ_{xy} = 50 and λ_z = 10, respectively. This variation in scale ratios results in a distorted-scale model with a distortion ratio of λ_{xy}/λ_z = 5, enabling greater flow depths and Reynolds numbers in the model. This approach enhances the accuracy of measurements and improves the dynamic similarity to the real-world prototype during simulations (Li et al., 2019). Since gravity forces play a dominant role in free-surface flows, Froude similarity, where $Fr_M = Fr_P$ (subscripts *M* and *P* refer to the scale *Model* and the real-world *Prototype*), allows the experimental model values to be scaled up to the real-world prototype (Chanson, 2004). This results in the following ratios for flow depth, velocity, discharge, and time:

$$\frac{d_P}{d_M} = \lambda_z \tag{1}$$

$$\frac{U_P}{U_M} = \lambda_z^{1/2} \tag{2}$$

$$\frac{Q_P}{Q_M} = \lambda_z^{3/2}\lambda_{xy} \tag{3}$$

$$\frac{t_P}{t_M} = \lambda_z^{-1/2}\lambda_{xy} \tag{4}$$

Here, *d* represents the water depth, *U* represents the flow velocity, *Q* represents the flow rate, and *t* represents time. The meanings of the subscripts are the same as explained earlier. Consequently, the model represented an urban block measuring 78 meters in length and 48 meters in width, with streets that are 7.5 meters wide, peak flood depths of approximately 0.6 meters, inflow discharge of 7.12 m^3/s and 3.16 m^3/s at Inlet1 and Inlet2 separately at prototype scale.

2.1.4 Measuring techniques

Electromagnetic flowmeters were installed in the pipes downstream of each outlet, enabling continuous measurement of flow rates. Flow depth measurements at selected locations within the physical model were carried out using ultrasonic distance-measuring sensors with measuring points shown in Figure S2. Surface flow velocities were assessed using a large-scale particle image velocimetry (LSPIV) method (Figure S3), following the approach described by Fujita et al. (1998). The validation process involved comparing surface velocities measured by LSPIV with near-surface and depth-averaged ADV velocities. The results indicated that LSPIV velocities were slightly lower than near-surface ADV data, likely due to tracer clogging. Table S2 in the supplement contains the measurement methods of the variables involved in the current laboratory experiments, as well as information on their respective resolutions. More details about the experimental setup and the methods are available in Mejía Morales (2022) .

2.2 Urban block configuration

In this study, 3D numerical simulations are carried out for the urban blocks for which the 2D simulations of Dewals et al. (2023) did not perform very well and for some more representative cases in which the 2D simulations performed well. The urban blocks that were simulated with the 3D model are depicted in Figure 1(b). In all cases, the maximum number of openings per side is three, as in configuration C19-12 (Figure 1b). Among the selected eight configurations, there is the control configuration C00-00, which has only streets and no urban blocks, the configuration C100-100, which does not include an urban block but only a large open space, and the configuration C19-12 with the most openings. The remaining configurations include configurations C00-04 and C00-12, which have varying numbers of openings on the same side, and configurations C1, C3, and C4, which have the same number of openings but in different locations.

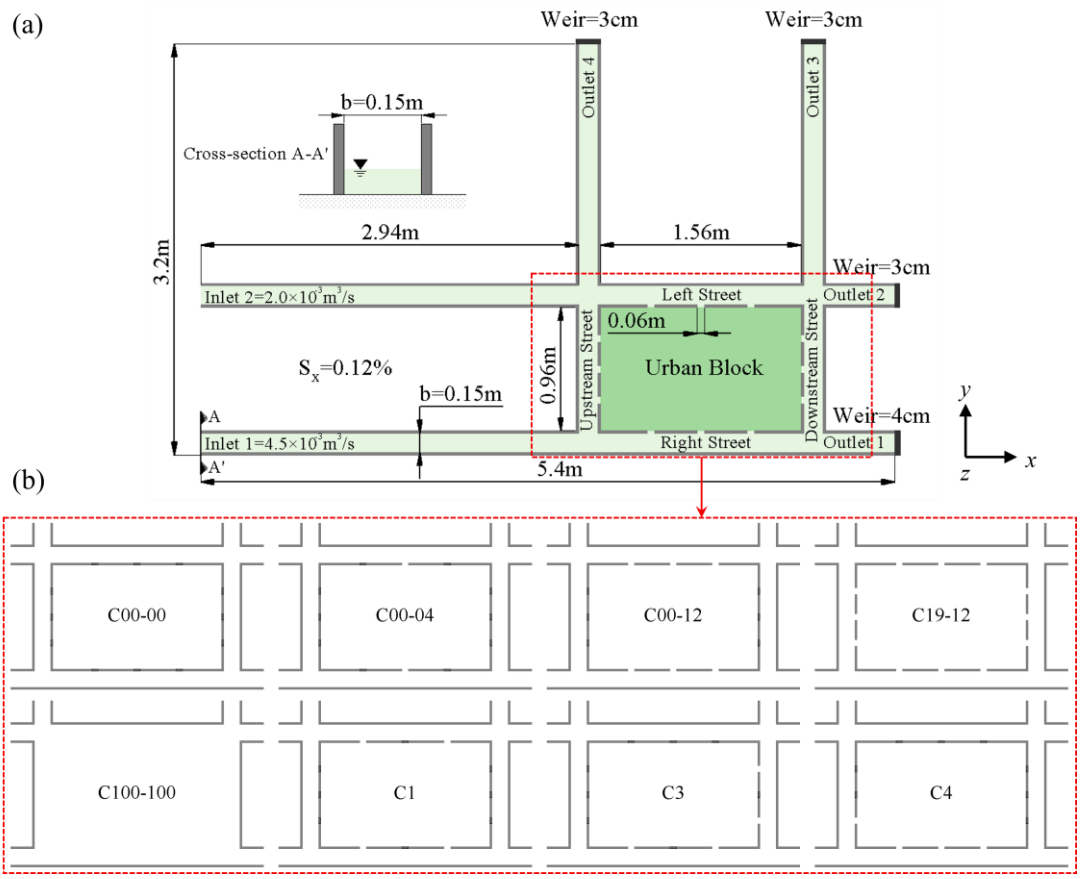

Figure 1 (a) Planview of the experimental setup; (b) the urban configurations that were simulated with the 3D model. The figure and the naming of the different urban block configurations is adopted from Mejía Morales (2022).

2.3 3D Numerical modelling

2.3.1 Model description

The experiments were reproduced by numerically solving the 3D incompressible Reynolds-Averaged Navier-Stokes (RANS) equations with OpenFOAM (v9). In conjunction with the Navier-Stokes equations, the continuity equation is applied. The interFoam solver was used and the *k-ω* SST turbulence closure model was implemented for the closure of the RANS equations. The latter was chosen because it has been used and validated for a broad range of engineering applications (Versteeg, 2007). The free surface was captured with the volume of fluid (VOF) method introduced by Hirt et al. (1981). This method is computationally efficient, and it is one of the most commonly used methods to model free surface flows and it has been extensively validated (Torres et al., 2022). The cells that contain only water or only air are assigned a value of *alpha.water* equal to 1 or 0, respectively. The interface between water and air is detected at the locations where *alpha.water* equals 0.5. A Courant-Friedrichs-Lewy (i.e., CFL) restriction

of 1 was imposed, which leads to an adjustable time step of the order of 0.002 s. The characteristics of the model are summarized in Table 2.

The 3D modelling results are compared with the experimental measurements as well as with 2D (depth-averaged) modelling results presented by Dewals et al. (2023). From the modelling results of Dewals et al. (2023), only those generated in code WOLF with 5 mm rectangular cells and a depth-averaged k-ε turbulence closure are used herein for comparison. More details about the 2D modelling approach can be found in Dewals et al. (2023).

2.3.2 Boundary conditions

Constant inflow discharges of 4.5 l/s and 2 l/s are normally imposed at the Inlet 1 and Inlet 2, respectively. The law of the wall is used to describe near-wall flow behaviour. The *nutkWallFunction* was applied to the bottom and side walls of the model, as well as to the weirs at the outlets. Due to the very small roughness in the physical experiment, and the adoption of a very small k_s in the 2D simulation (3.6×10^{-5} m), the *nutkWallFunction* by default assumes that the walls are smooth, which means the wall roughness parameter is set to zero. The geometry used in the 3D model is extended, compared to the experimental setup, for 0.2 m downstream of each outlet to allow a proper schematization of the weirs. The initial flow depth of each simulation is set to 0.05 m. Although the model boundary conditions are steady, the computational results (i.e., flow depths, discharge, velocities) show some fluctuations at certain locations, which were also observed in the laboratory experiments. InterFoam is an unsteady solver, therefore, all simulated results were averaged over a period of 100 s. The averaging period did not include the initial time until the model stabilized its flow pattern from the initial flow conditions. This initial time period that was not included in the time-averaging was 100s. As shown in Figure S4 and Figure S5 in Supporting Information, this results in smoothing out minor fluctuations, which remain small compared to the quantities of interest.

Under the boundary conditions set in the current model, including inflow discharge and downstream water level, although these conditions were manually configured, they are consistent with real flood scenarios, as further validated by the non-dimensional numbers

calculated, which provide important insights. Non-dimensional numbers are used to compare the hydraulic conditions in the CFD model with those observed in real case scenarios. Under the current simulation conditions, the average Reynolds number in model stabilization is 1.14×10^4. For Reynolds number, values below 2000 indicate laminar flow, dominated by viscous forces. While values above 4000 suggest turbulent flow, characterized by chaotic and irregular fluid motion. With Re = 1.14×10^4, the flow is firmly in the turbulent regime. The average Weber number is 55.20. For Weber number, values below 1 suggest that surface tension forces dominate, maintaining fluid stability, values above 10 indicate that inertial forces overpower surface tension, leading to fluid deformation or fragmentation. A Weber number of 55.20 suggests that inertial forces are significant, making surface deformation likely. The model's average Froude number is 0.31, which is consistent with flow characteristics commonly observed in urban floodplain scenarios during flood events.

Table 2 Numerical implementation of the 3D model in OpenFOAM (v9) and prescribed boundary conditions

Implementation	
Solver	interFOAM
Turbulence model	RANS k-ω SST
Wall treatment	nutkWallFunction
CFL number	< 1
Multiphase model	VOF
Interface capturing scheme	MULES scheme
Pressure-velocity coupling	PISO scheme
Boundary conditions	
Inlet	flowRateInletVelocity
Outlet	pressureInletOutletVelocity
Atmosphere	pressureInletOutletVelocity

2.3.3 Meshing strategy

Structured mesh was chosen to build the computational domain, including the street branches and the block area (Figure 2). In the current study, all cells in every 3D mesh are hexahedra with same dimensions in all three directions. To select a suitable mesh for simulating flow intrusion into buildings in urban areas, mesh sensitivity tests were carried out for the

configuration C4 by testing three meshes with cell sizes of 4 mm, 5 mm, and 10 mm. With these cell dimensions, the openings are covered by 15, 12 and 6 cells, respectively. In each meshing test, all the other parameters of modelling were kept the same. The simulations were run in parallel using the public domain OpenMPI implementation of the standard MPI on Guangxi University's high-performance computing platform, which is powered by the Sugon 7000A high-performance super-parallel computer system. A total of 100 cores are utilized for these simulations. The number of cells is 6.5×10^6 for 4 mm, 3.3×10^6 for 5 mm, and 0.4×10^6 for 10 mm.

The discharge partitions and surface flow patterns that were generated with different mesh sizes are presented in Figure S6 and Figure S7. When drawing the flow pattern diagram, a sufficiently detailed data resolution is necessary to capture a complete recirculating structure. When considering resolution, the 5 mm grid performs better than the 10 mm grid. Besides, in the 2D simulation study by Dewals et al. (2023), a 5 mm grid was used for the simulation. Therefore, this study will also prioritize a 5 mm grid model. Additionally, the discharge partitions of the model with a cell size of 5 mm are very close to the results of the model with a cell size of 4 mm, with a maximum difference of less than 0.5%. Therefore, the mesh size of 5 mm was selected to simulate all the tested configurations to reduce the computational burden. The computational time to simulate 200 s of flow with 100 cores was about 20 h for each case. Furthermore, the mesh sensitivity analysis of the 2D model was detailed by Li et al. (2020) and Dewals et al. (2023).

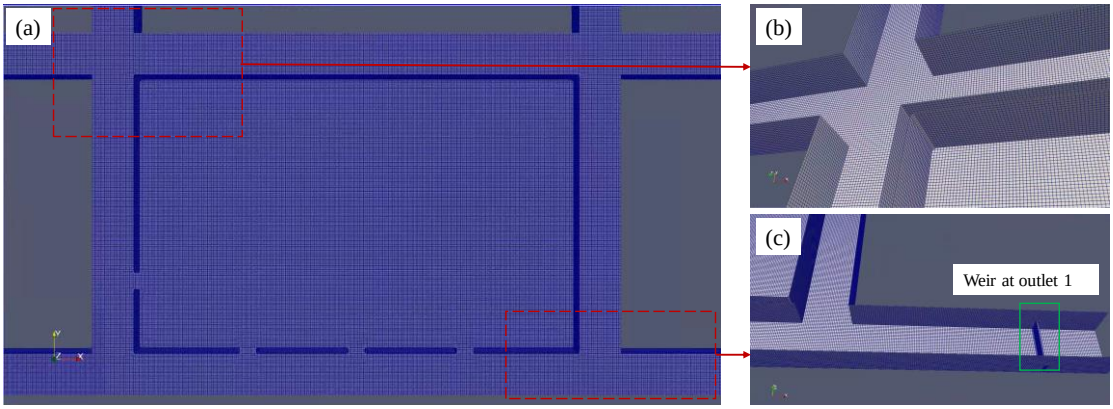

Figure 2 Model configuration of the case C4. The mesh consists of square cells with horizontal and vertical resolution of 5 mm, (a) is a top view of the study area, (b) is a schematic diagram of the intersection, and (c) is a schematic diagram of the outlet with an overflow weir.

3 Results

3.1 Flow depth

Figure 3 shows the flow depth maps observed in the laboratory and predicted by the 3D and 2D computational models for three representative configurations: C00-00, C100-100 and C19-12. The flow depth maps for the rest of the configurations are presented in Figure S8. The profiles of flow depths along the central lines in the streets around the blocks are presented in Figure 4 (C00-00 and C19-12) for a quantitative analysis.

The Right street has greater flow depths than the other streets due to the higher flow rate at Inlet 1 compared to Inlet 2 and the greater weir height at Outlet 1 than at the other outlets. Consequently, the geometry and inflow conditions generate a maximum water depth near Outlet 1, with a gradual decrease towards the Upstream and the Left street. Maximum variations in flow depth within each configuration are approximately 2 cm. The water depth gradually increases within the block from the upstream to the downstream area and there is no significant depth variation along the *y*-direction. Both the 3D and 2D models reproduced well all the observed flow depth variations.

Local variations of flow depths close to street intersections are well reproduced by the 3D model (Figure 4). The water level fluctuations that were observed in the experimental model, especially for the configurations C00-00, C19-12, C00-04, C1, C3 (Figure S8), were not reproduced by the 2D model but are well reproduced by the 3D model (Figure 4 a and e).

306 Overall, the discrepancies between the observed and predicted flow depths are small, with
307 differences limited to ±2 mm (i.e., ~2%). When compared to the 2D modelling results, the flow
308 depths predicted by the 3D model are slightly more accurate regarding the flow depth at outlets
309 and depth variation in the right street as displayed in Figure 4.

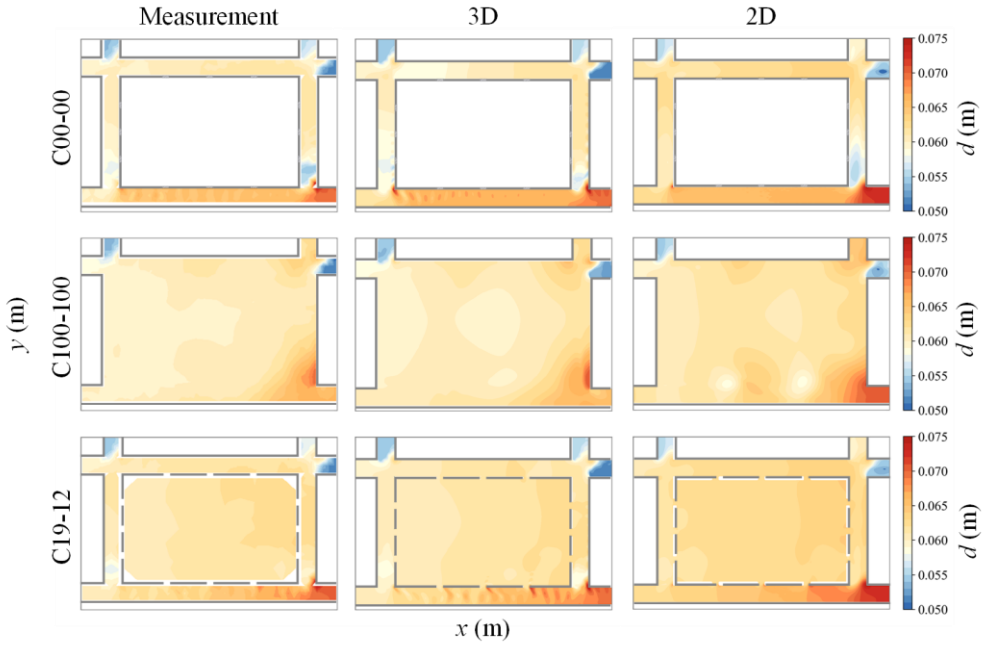

310
311 Figure 3 Flow depths observed in the laboratory and predicted by the 2D and 3D models for
312 the configurations C00-00, C100-100, and C19-12. The flow depths measured in the laboratory
313 and computed by the 2D model were firstly published by Mejía-Morales et al. (2021), and
314 Dewals et al. (2023), respectively.

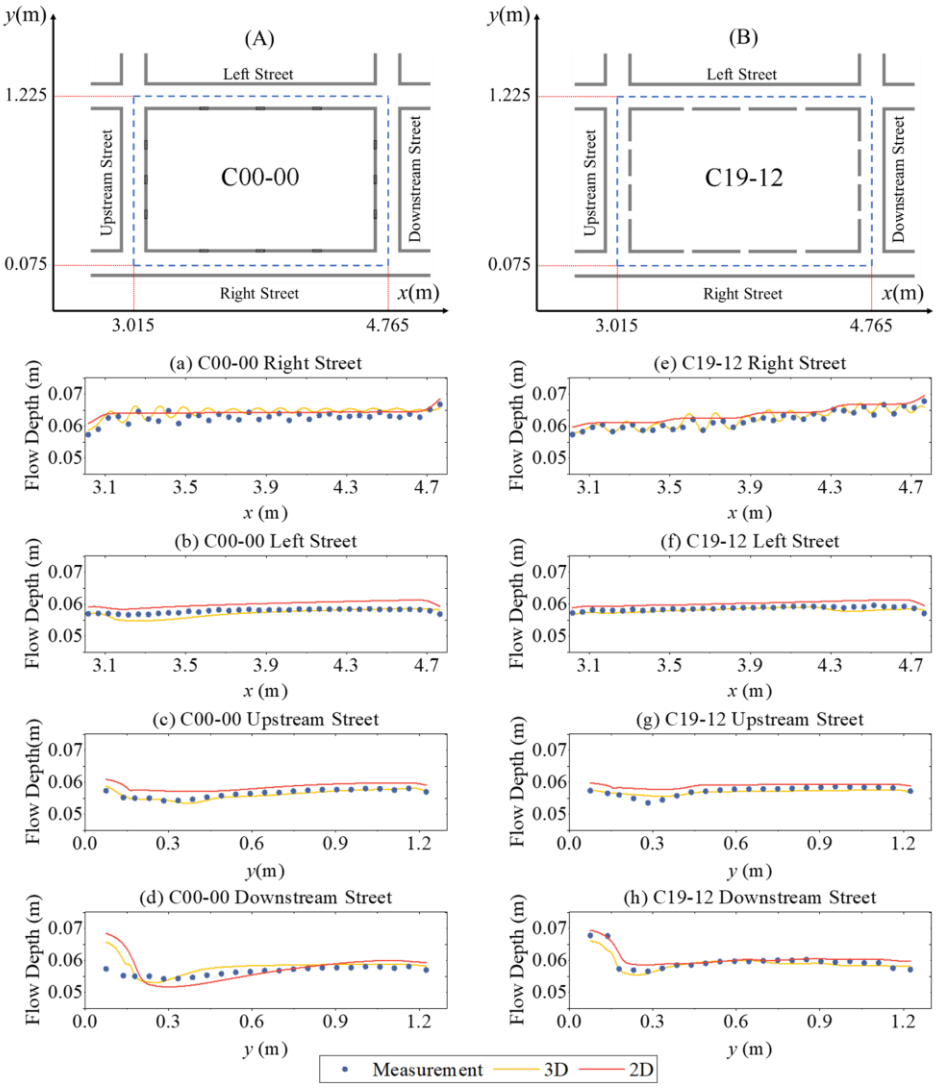

Figure 4 Flow depth profiles along the centerlines of the Right street, Left street, Upstream street and Downstream street (Figure 1) for the cases C00-00 (a-d) and C19-12 (e-h).

3.2 Flow discharge partitioning at the outlets and in-between streets

Figure 5 compares the modelled outflow discharge distribution, Q_R (%), at the four outlets to the experimental results. The error bars represent the experimental uncertainty and standard deviation of the numerical results, respectively. The differences between the experimental and numerical results of the outflow discharge distribution are reported in Figure 6 in terms of percentage points and root mean square error (RMSE). According to the experimental results, the outflow discharge through Outlet 1 (Q_{R1}) is the largest in all tested configurations except in configuration C100-100. The portions of the outflow discharges decrease in the order $Q_{R1} > Q_{R2} > Q_{R3} > Q_{R4}$ (except for configuration C100-100). This trend of discharge repartition is successfully reproduced by the 3D model. The values of Q_{R2} and Q_{R3} simulated by the 3D model

are remarkably close to the laboratory observations with differences lower than 0.5 pp (i.e., percentage points). Nevertheless, the 3D model underpredicts Q_{R1} by about 1.2 pp for all tested configurations, leading to a slight overestimation (~1 pp) of Q_{R4}. The decreasing trend from Q_{R1} to Q_{R4} is less well reproduced by the 2D model. Specifically, Q_{R2} and Q_{R3} computed by the 2D model are systematically lower than the experimental observations by ~1 to ~2 pp, while Q_{R4} shows a significant overestimation (2.5-3.9 pp), disrupting the overall trend. The RMSEs displayed in Figure 6b highlight that the discharge partitions predicted by the 3D model (RMSE<1 pp) are systematically more accurate than those of the 2D model (RMSE of 1~2 pp). Most deviations between the numerical and experimental results were within the range of experimental uncertainties, which is about 1.5% as reported by Mejía-Morales et al. (2021). However, the deviations show clear trends in terms of overestimation or underestimation, so the evaluation of the relative performance of the model, regarding flow discharge partition still stands (Figure 6a).

Configuration C100-100 is a special case, with solely an open space in the middle of the street networks. The partition of outflow discharges observed in the laboratory ($Q_{R3} > Q_{R2} > Q_{R1} > Q_{R4}$) is again well predicted by the 3D model with differences smaller than 1 pp for Q_{R3} and Q_{R2}. This is a substantial improvement compared to the predictions of the 2D model, which provides not only a less accurate discharge partition but also a completely different ranking of the magnitudes of the outlet discharges ($Q_{R1} > Q_{R4} > Q_{R2} > Q_{R3}$), with a maximum difference of ~6 pp at the Outlet 3 and a RMSE of 4.5 pp.

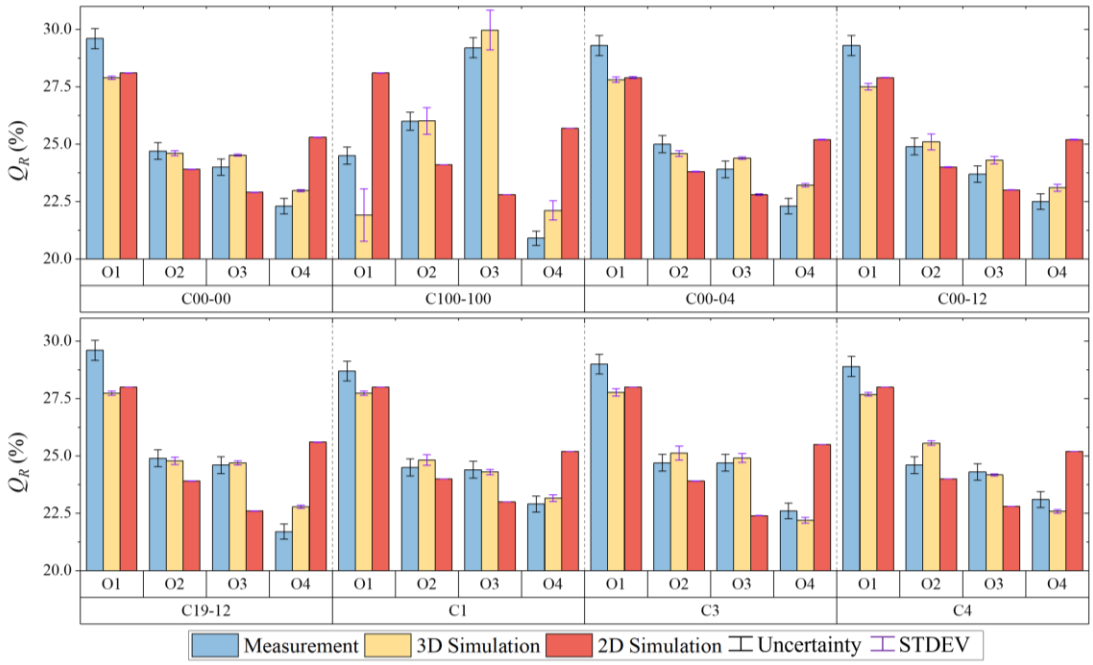

Figure 5 Measured and modelled discharge partition at the four outlets for all configurations of Figure 1 (also presented in Table S3). O1, O2, O3, O4 refer to the Outlets 1, 2, 3, 4, respectively. The error bars of the numerical and experimental results represent the standard deviation during the modelling duration and the experimental uncertainty, respectively.

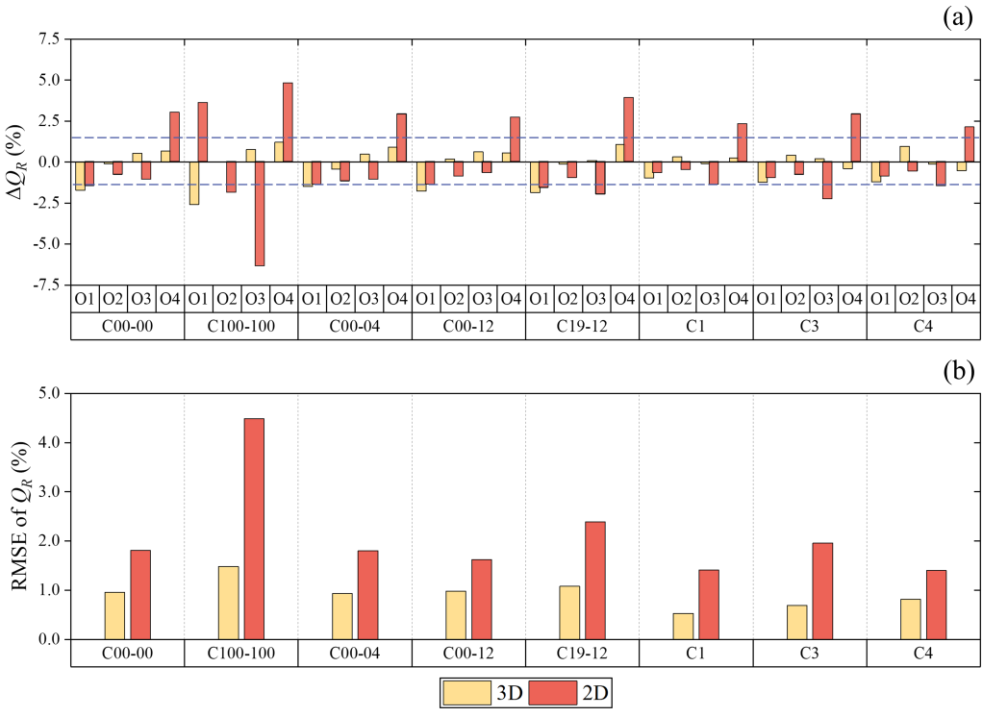

Figure 6 (a) Differences between the numerical and experimental outflow discharge partition at the four outlets in percentage points (pp) (also presented in Table S2), the dash lines highlight a difference of ±1.5 pp associated with the experimental uncertainty; (b) RMSE between the numerical and experimental outflow discharge partition at the four outlets in percentage points (pp).

3.3 Horizontal flow velocity patterns (surface velocity & depth-averaged velocity)

Flow patterns in the streets and inside the block are shown in Figure 7. The flow velocity

magnitude and the corresponding streamlines are presented. The first and second columns show the surface velocity (magnitude along the *x* and *y* directions) measured in the laboratory ($U_{S,\ Exp}$) and predicted by the 3D model ($U_{S,\ 3D}$). The third and the fourth columns represent the depth-averaged velocity simulated by the 3D model ($U_{D,3D}$) and the 2D model ($U_{D,2D}$). The value of $U_{D,3D}$ is the magnitude velocity of *Ux*, *Uy* and *Uz* averaged with all grid layers along the *z* direction.

3.3.1 Flow pattern in the streets

Two four-branch crossroads and two T-bifurcation crossroads are present in all configurations, except C100-100. Flow recirculation in the streets generally occurs at the flow separation zone at the crossroads. These patterns are well reproduced by both the 2D and the 3D modelling approaches for most of the cases. For example, when the Right street meets the Downstream street, there is flow separation in both streets. The flow separation in the Downstream street occurs due a combination of the high flow inertia and the adverse pressure gradient due to the flow expansion. The flow separation in the Right street, near Outlet 1, is owed to the adverse pressure gradient due to the flow depth increase near the weir. Both models capture these flow patterns well. Besides, the high flow velocity in the Right street has a large influence on the flow patterns inside the porous blocks. This is analyzed in the next section. Both models successfully reproduce the flow patterns observed at the junctions where the Left street meets the Upstream or Downstream streets. Due to the lower flow velocity in the Left street compared to the Right street, flow contraction occurs near the junctions, resulting in the discharge being concentrated along one wall with limited mixing. However, the degree of contraction is not highly pronounced.

The 3D model produces small recirculation zones at the Upstream street near the connection with the Right street, which are not always observed to that extent in the experiments. Overall, the measured and computed flow surface patterns in the streets match well in both 2D and 3D models.

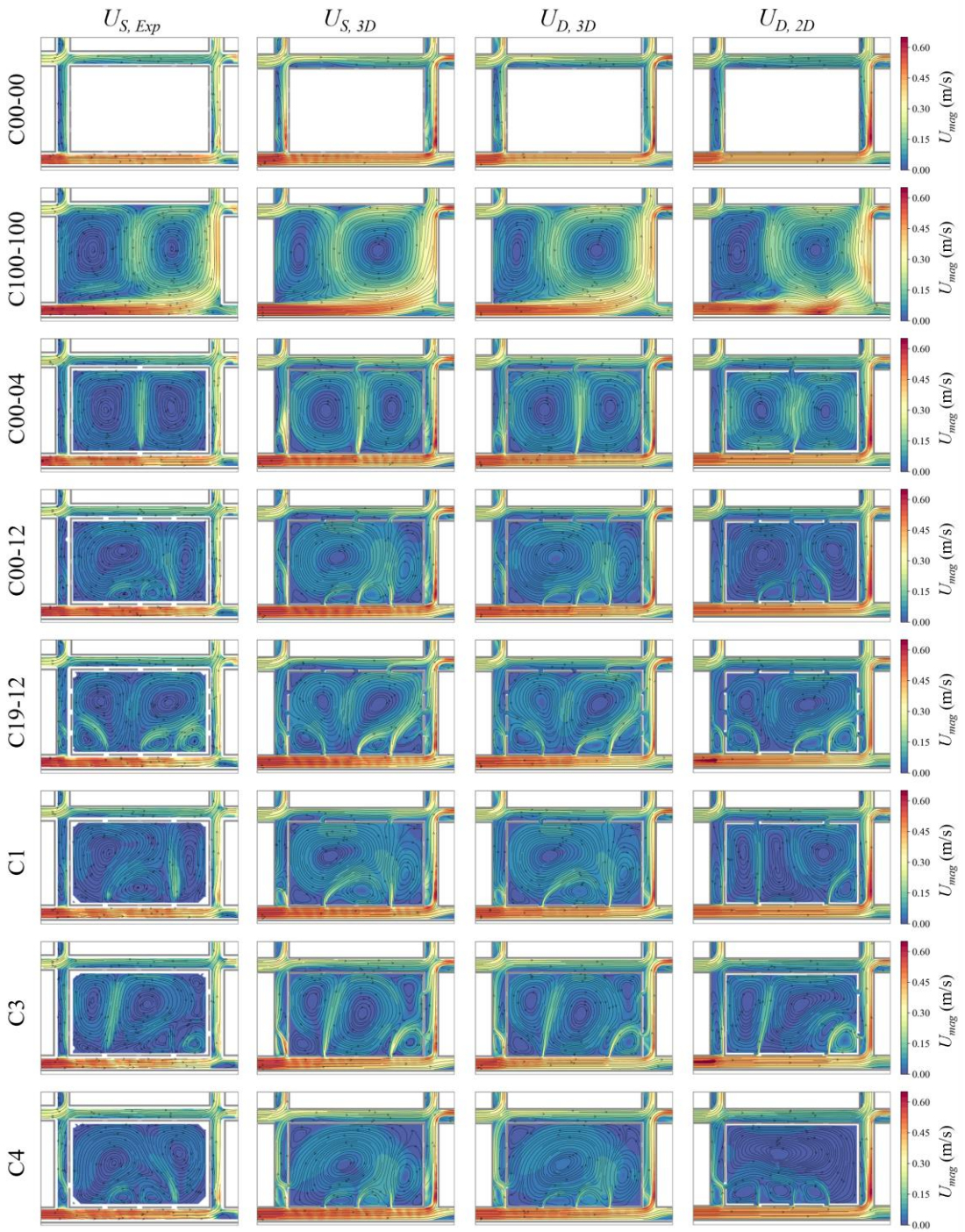

Figure 7 Time-averaged surface velocity field (m/s) in the tested urban configurations measured in the laboratory ("$U_{S,\,Exp}$") and computed by the 3D model ("$U_{S,\,3D}$"); Depth-averaged velocity field (m/s) in the tested urban configurations computed by the 3D model ("$U_{D,\,3D}$") and by the 2D model ("$U_{D,\,2D}$"). The first and fourth columns are adapted from Mejía-Morales et al. (2021) and Dewals et al. (2023).

3.3.2 Complex flow patterns inside the porous blocks (surface velocity)

The number and locations of openings are varied in each porous configuration, directly affecting the complex flow patterns formed inside the porous blocks, particularly in terms of the size, directionality, and relative positioning of the recirculation zones. Table 3 provides a

qualitative comparison of the flow recirculation zones observed in the experiments and the numerical modeling, based on the flow surface velocity fields illustrated in Figure 7.

First, both the 3D and the 2D models generate the correct number of observed large flow recirculation zones, although there are some variations in the shape or size of these recirculation zones. For example, two symmetrical counterrotating recirculation zones are observed in the C100-100 experiments, but the predicted recirculation zones are not equal in size, both in the 2D and 3D numerical simulations. Besides, by visualizing the flow recirculations in all configurations with openings (i.e., based on the flow surface velocity $U_{s,3D}$), it can be concluded that the openings in the Right street have the largest influence on the flow recirculation patterns inside the blocks. This is due to the greater flow depth in the Right street induced by the larger weir height in Outlet 1, and the resultant pressure gradient that is induced along the *y* direction. The 3D model reproduces more accurately than the 2D model the large recirculation zones. This could be the result of a more accurate simulation of the jet formation at the openings of the Right street under the combined effect of the fast flow in the Right street and the pressure gradient due to the water level difference, as well as a more accurate estimation of the dissipation of the jet due to turbulent mixing in the shear layers that are formed after each jet enters the open space within each porous block.

Small recirculation zones are mostly generated by the flow jets injecting from the Right street or formed at some corners of the porous block. The performance of the 3D model in simulating relatively small recirculations is fairly good for most configurations, and especially for Configuration C00-12. The directionalities of flow jets originating from the Right street vary in different configurations. Most of these directionalities are perfectly captured by the 3D model, except for the openings located in the downstream part of Configurations C3 and C4 (Figure 7).

The even smaller recirculations mostly appear at the block inner corners or they attach to larger recirculations, and they are the most challenging flow patterns to capture with the numerical models. The smaller recirculations are successfully reproduced by the 3D simulations only in

Configurations C00-12 (observed at the two corners near the Right street), and C4 (observed at the downstream corner near the Right street). However, such small recirculation patterns have hardly any effect on the overall flow compared to the large recirculation patterns.

Table 3 Qualitative appraisal of the agreement between observed and computed flow patterns inside the central block. Notation "L" stands for "large recirculation(s)", "S" for "smaller recirculation(s)" and "s" for "even smaller recirculation(s)".

Configurations	$U_{S,\,Exp}$ (1)	$U_{S,\,3D}$	$U_{D,\,3D}$	$U_{D,\,2D}$(1)
C100-100	2L	2L	2L	2L
C00-04	2L	2L+3s	2L+3s	2L
C00-12	2L+2S+3s	2L+2S+3s	2L+2S+3s	2L+3S
C19-12	2L+3S	2L+3S	2L+3S+1s	2L (incorrect relative sizes) + 3S
C1	3L	3L+1S+2s	3L+1S+2s	4L (incorrect shape)
C3	2L+2S+3s	2L+3S+1s	2L+3S	2L+2S
C4	2L+2S+1s	2L+3S+1s	2L+3S+1s	1L+5S (incorrect shape)

(1) Obtained from Dewals et al. (2023).

Flow surface velocity profiles are also compared at some cross-sections along the x and y directions. Taking the Configuration C4 as an example, Figure 8 shows the computed surface velocity profiles inside the block normal to the lines at x = 3.5 m, 3.89 m and 4.28 m; y = 0.24 m, 0.5 m and 0.75 m (the coordinates of the cross sections are shown in Figure S9). This allows to quantitatively evaluate the locations and sizes of flow recirculation. First, the simulated velocities U_y of the flow jets close to the openings match well the observations, as shown by the peaks in Figure 8a. Additionally, although the velocities are small (U_x or U_y < ~0.075 m/s), the computed velocities generally align very well with the experimental measurements regarding the distribution of positive and negative velocities (i.e., directions of recirculation) as well as the location of zero velocity (i.e., centers of recirculation). Combined with the previous qualitative and quantitative analyses, the performance of the 3D model for predicting surface flow patterns is very good. In addition, although the results from the 2D model also agree fairly well with the experimental results, the 2D model is based on depth-averaged shallow water

equations and thus does not provide actual surface velocities. The 2D model results represent depth-averaged velocities, which can lead to lower accuracy in capturing detailed flow structures compared to the 3D model (e.g.-Figure 8f).

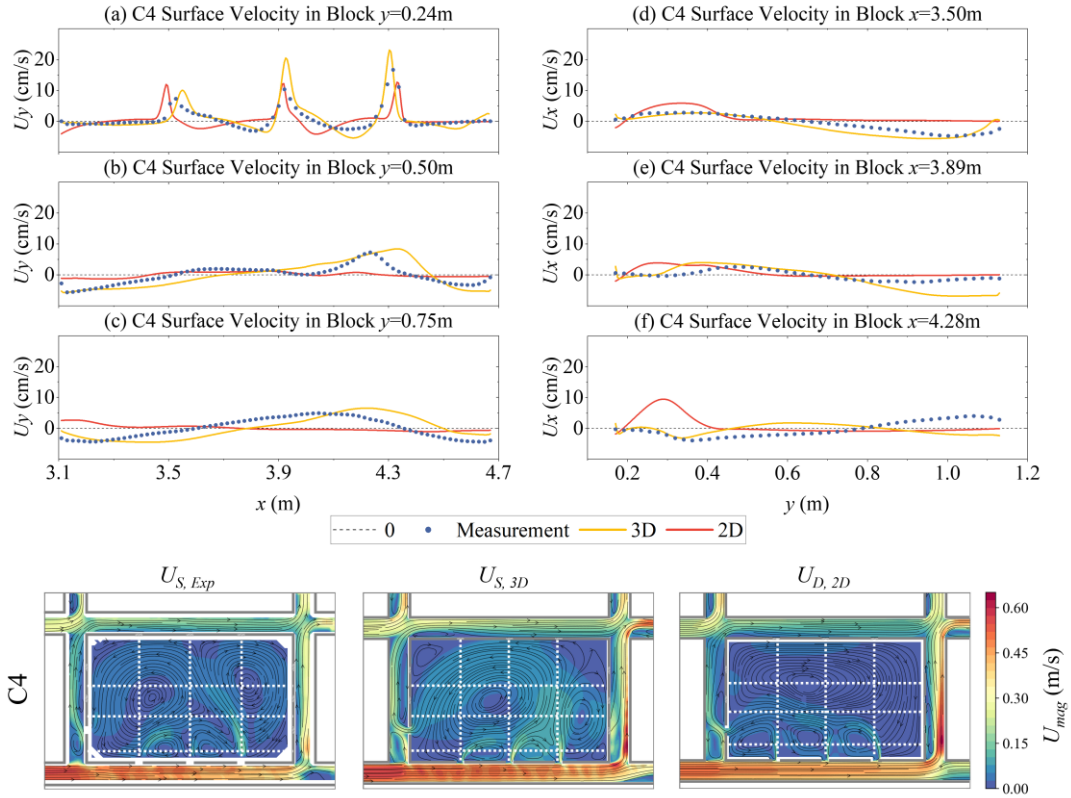

Figure 8 Surface velocity profiles of 3D model inside the porous block at various cross-sections for the configuration C4, (a-c): the velocity U_y normal to the lines at y = 0.24 m, 0.5 m and 0.75 m; (d-f): the velocity U_x normal to the lines x = 3.50 m, 3.89 m and 4.28 m. Each cross-section has been marked on the flow pattern plots of C4 in white dashes (also marked using coordinates in Figure S9.).

3.3.3 Comparison between 2D and 3D depth-averaged flow patterns

As described in Dewals et al. (2023), the 2D modelled flow patterns within the porous blocks in the first test series (C00-04, C00-12, and C19-12 in this study) agree well with the measurements in terms of number and direction of the recirculation zones. Assuming that the measured surface flow field is representative of the depth-averaged flow field, the depth-averaged velocity patterns obtained from the 3D models, $U_{D,3D}$, are more accurate compared to the 2D modelling outputs. In the case C00-04, the performance of the two models is similar, and the modelled velocities agree well with the measurements; however, the velocity simulated by the 2D model is overestimated. In the case C19-12, the large flow recirculation close to the Downstream street predicted by the 2D model is larger than that produced by the 3D model,

with the latter being closer to the measurements.

Based on the results of Dewals et al. (2023), the 2D model underperforms in accurately predicting the shape and size of the recirculation zones for some configurations, particularly in the cases with asymmetrical openings (C1, C3, and C4). In the measurement of Configuration C1, a large recirculation is generated in the upstream part of the block, occupying about two-thirds of the block area, and a relatively narrow recirculation with a clockwise directionality is produced at the right side of the downstream flow jet. These features are accurately reproduced by the 3D model, but missed by the 2D model. The latter produces flow patterns with two narrow flow recirculations at the upstream side and a relatively large circular recirculation. Similarly, the round shapes of the large flow recirculations observed in the experiments for Configuration C3 are well predicted by the 3D model, but the large recirculations presented by the 2D model are too elongated, while the small recirculation produced in the left corner in the downstream area is only reproduced by the 3D model (Figure 7).

Configuration C4 was the most challenging case for the 2D model. Both the 2D and 3D models failed to reproduce the two large recirculations on the right side (Figure 7). However, the flow pattern of the 3D model still exhibits two large recirculations with the right direction, only the ratio of the sizes differs from the measurements. On the contrary, the results of the 2D model show a large recirculation occupying most of the block area, with small recirculations near the openings to the Right street, while the velocity within the block was obviously underestimated.

3.4 Cross-sectional velocity distribution

3.4.1 Cross-sectional velocity patterns

Figure 9 presents a cross-sectional view of iso-velocity contours (velocity component normal to the cross-section) measured in the laboratory (left column) and computed by the 3D model (right column), combined with the secondary currents of configuration C19-12. Similar iso-velocity contours from C00-00 and C4 (i.e., the configuration without opening and the configuration with the most modelling challenges) are also presented in the Supplementary Material (Figure S11, Figure S12). The following analysis will consider C19-12 as an example,

but the findings from this case are similar to those from the rest of the cases.

The vertical variation of the streamwise velocity at cross-sections of the Right street exhibits complex patterns. Significant velocity variations in the z-direction (U_z) are observed in the cross-sections at x = 3.3 m, 3.69 m, and 4.44 m along the Right street in the experiments (Figure 9), with the highest flow velocity close to the flow surface in the middle of the street and decreasing toward the bottom. The 3D model not only replicates the boundary layer structure along the z direction but also successfully captures the contour shapes.

In the Left street, there is a velocity gradient from one side of the street to the other, which is well reproduced by the 3D model. A similar horizontal velocity gradient is also observed in the sections of the Downstream street, which is distinguished by higher velocities near the side wall. These features are fairly well captured by the 3D model. Nevertheless, negative zones are numerically reproduced near the street wall for the Left street and Downstream street, but this is hardly observed in the experiments. Actually, negative velocity indicates reversed flow direction of the streamwise velocity that may refer to flow recirculation in the horizontal plane (Figure 7, $U_{S,3D}$ of the case C19-12), which is generated by flow separation.

The computed secondary flow currents are also provided in Figure 9 and Figure 10 with the flow velocities being parallel to the cross sections (U_x & U_z or U_y & U_z). Secondary flow currents are observed at some sections close to the bottom such as the sections x = 4.44 m of the Right street and Left street and y = 0.75 m of the Downstream street. The flow velocities U_z at two adjacent sections of the Right street are reversed, water flows down to the bottom from the surface at section x = 3.3 m but goes up from bottom to surface at section x = 3.69 m. By referring to the flow depth profiles in Figure 4 and flow horizontal patterns as presented in Figure 7, this variation of flow direction may be related to the fluctuations of the surface. Overall, the flow secondary currents are not very strong, with the water moving in the horizontal directions (i.e., x or y directions), such as the sections x = 3.3 m, 3.69 m of the Left street and the section y = 0.51 m of the Downstream street.

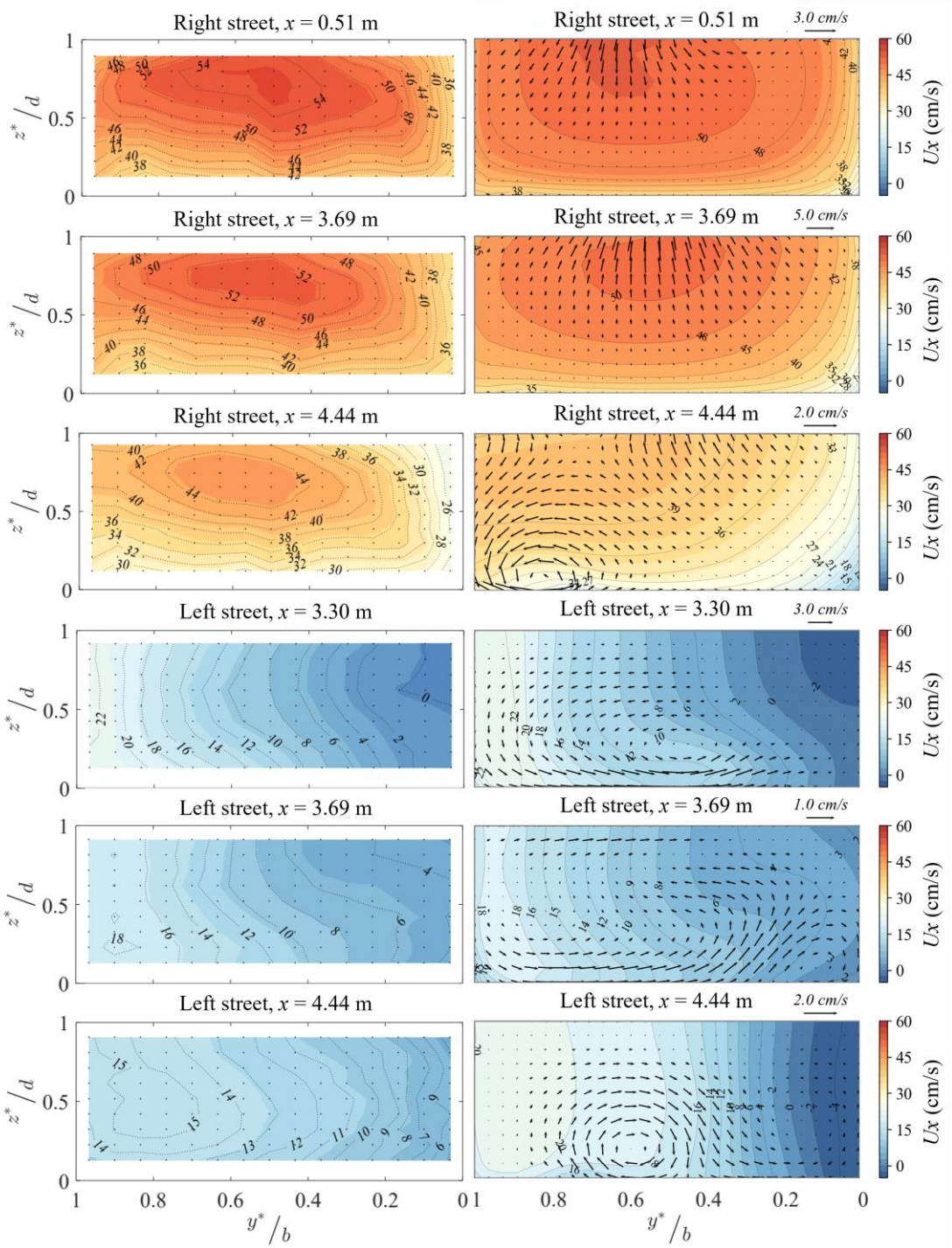

Figure 9 Velocity field (U_x) at the street cross section of Right street and Left street for the configuration C19-12, observed in the laboratory (left row) from the upstream toward downstream and computed by the 3D model (right row). The *x* and *y* axes are normalized by the street width b and the z axis is normalized by the local flow depth. The contour filled plot in the right row is drawn with the velocity normal to the section (U_x or U_y), and the quiver plot is drawn with the two velocities parallel to the section (U_x and U_z or U_y and U_z). The experimental results (left row) are presented in the Mejía Morales (2022). Locations of these cross sections are explained in Figure S10.

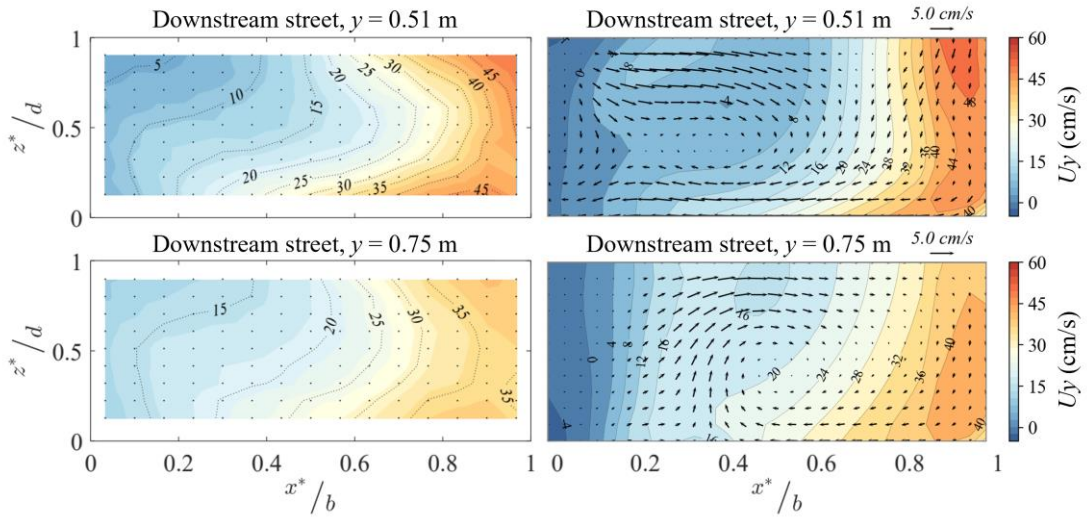

Figure 10 Velocity field (U_x) at street cross-sections of the Downstream street for the configurations C19-12, observed in the laboratory (left row) from the upstream toward downstream and computed by the 3D model (right row). The *x* and *y* axes are normalized by the street width *b* and the *z* axis is normalized by the local flow depth. The contour filled plot in the right row is drawn with the velocity normal to the section (U_x or U_y), and the quiver plot is drawn with the two velocities parallel to the section (U_x and U_z or U_y and U_z). The experimental results (left row) are adapted from Mejía Morales (2022). The locations of these cross sections are explained in Figure S10.

3.4.2 Distribution of vertical flow velocities

To further analyse U_z (a velocity component specific to the 3D simulations), the maps of U_z across horizontal slices from the 3D simulations are presented in Figures 11 and 12. Taking the Configuration C19-12 as an example (Figure 11), U_z is relatively small compared to the velocity magnitude U_{mag} in most of the area of the model across all 12 slices, but it remains significant (exceeding 20% of the U_{mag}) in many flow jets and separation zones. U_z is particularly pronounced in mid to lower layers (z = 0.01 to 0.03 m) when comparing different slices.

Figure 12 displays the normalized vertical velocity maps at z = 0.03 m for the eight selected configurations. U_z is of considerable magnitude in the flow areas with jets and flow separation zones. Specifically, a red zone (i.e., positive flow) and blue zone (i.e., negative flow) are generally observed close to the same opening, which reveals reversed flow direction along the *z* axis in these areas. In most other areas, U_z remains relatively low (below 10% of U_{mag}). However, upon examining the large open space of the urban block, it can be observed that the map of normalized U_z velocities qualitatively matches the horizontal flow patterns of each configuration (Figure 7), indicating a correlation between the variation of U_z across the

horizontal plane and the flow recirculations. Such results suggest that U_z not only plays a significant role in shaping flow vertical structures within narrow channels (i.e., streets) (Figure 9), but also has a certain impact on flow structures in large open spaces of urban blocks with lower flow velocities. This is especially true when the flow pattern is heavily influenced by flow jets, emphasizing the importance of U_z in reproducing flow structures and thus the necessity to use 3D models instead of 2D models.

In summary, vertical velocity has had a certain impact on flow velocity and flow patterns in this model. However, since its overall magnitude is relatively small, it has not significantly affected the water pressure in the model. The water pressure still follows a linear hydrostatic distribution along the direction of gravity (Figure S14).

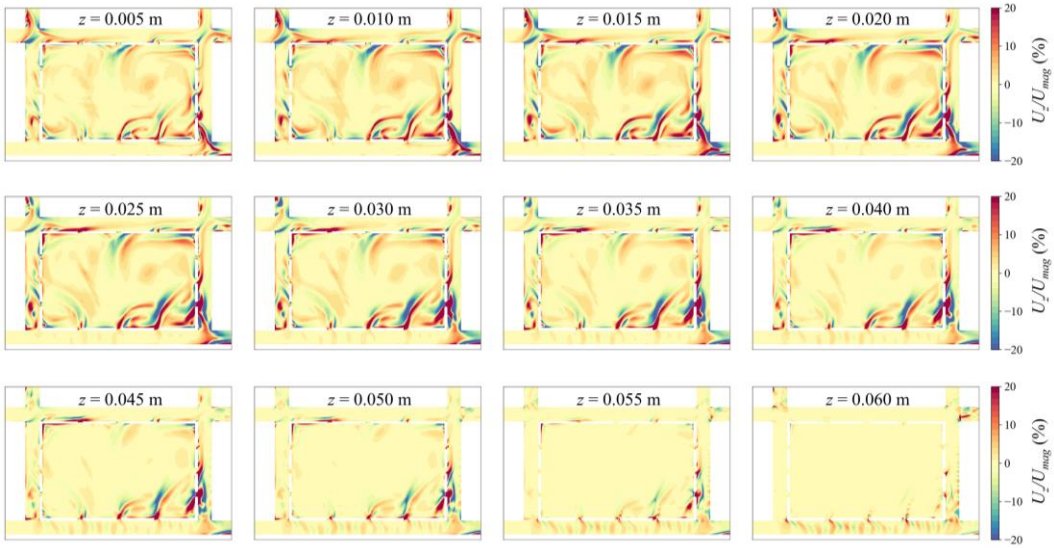

Figure 11 Maps of vertical velocity U_z simulated by the 3D model at various locations of the case C19-12. U_z is normalized by U_{mag} in percentage.

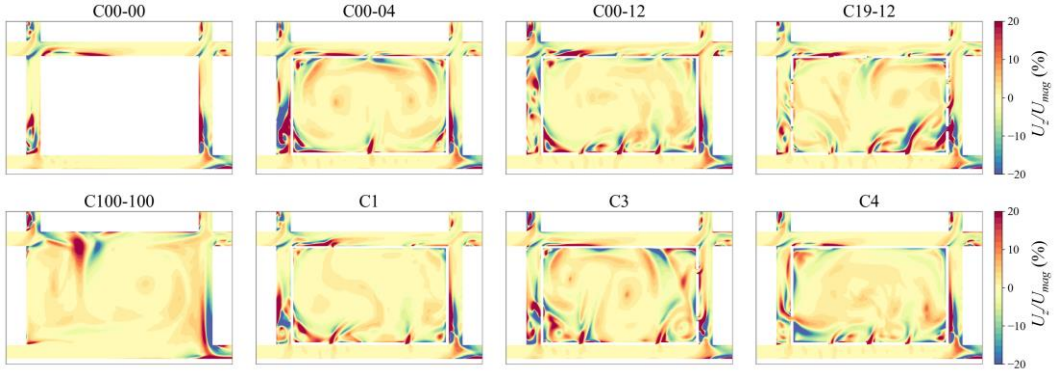

Figure 12 Maps of vertical velocity U_z simulated by the 3D model for the eight selected configurations at z = 0.03 m. U_z is normalized by U_{mag} in percentage.

4 Discussion

4.1 Horizontal flow velocity patterns in different layers

The depth-averaged flow pattern of the 3D computational simulation is obtained by averaging the extracted horizontal flow patterns from different layers. The differences between the horizontal flow patterns at the different layers is also important to analyze the three-dimensional structure of the flow. Figure 13 illustrates 12 layers of horizontal velocity patterns, taking C19-12 as an example. It can be observed that the flow velocity in the Right street increases from the bottom to the free surface, consistent with the previous analysis of vertical velocity profiles and the boundary layer theory. It is noteworthy that in the Downstream street near Outlet 1, a "Y" shaped bifurcation appears from the bottom upwards, with a noticeable weakening at the z = 0.025 m layer and disappearing at the z = 0.035 m layer, providing further evidence of the three-dimensional structural characteristics of water flow within streets. In the large open space of the urban block, the positions of various types of recirculations (recirculating centers) remain almost unchanged, while there are slight changes in the horizontal velocity of flow jets. In the layer closest to the bottom at z = 0.005 m, the vertical flow velocity significantly decreases, and various recirculations also exhibit noticeable distortions.

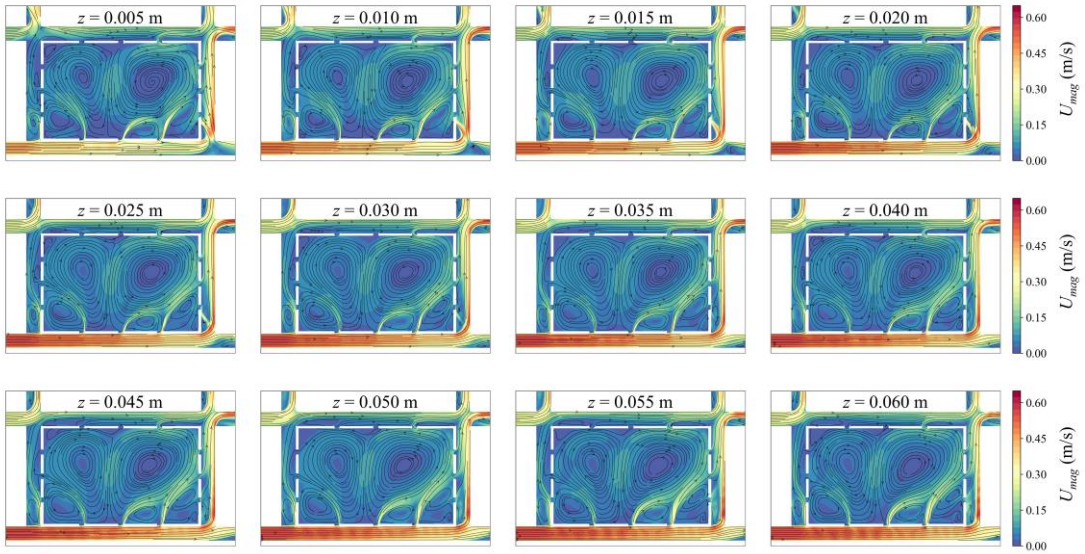

Figure 13 Horizontal flow velocity patterns across the depth from the 3D modelling for the configuration C19-12.

4.2 Difference between surface velocity and depth-averaged velocity in 3D models

The depth-averaged and surface velocity fields of the 3D model are compared in Figure 7 and

586 the differences in velocity magnitude between surface and depth-averaged flow are illustrated
587 in Figure 14. The major differences between surface velocity $U_{S,3D}$ and depth-averaged velocity
588 $U_{D,3D}$ are found inside the porous blocks, particularly in areas of flow recirculation. In
589 comparing the edge of recirculations, the velocity magnitude of surface flow is higher than the
590 depth-averaged velocity, as clearly presented in C00-12. On the contrary, at the center of
591 recirculations, the surface flow velocity is evidently lower than the depth-averaged velocity in
592 cases C00-12, C19-12, C1, and C4. Conclusively, based on these observations, the structure of
593 recirculations in depth-averaged flow appears to be smoother than that in surface flow under
594 steady flow. The flow patterns of the surface velocity and the depth-averaged velocity are very
595 similar regarding the form and size of the large and small recirculation patterns as well as the
596 location of the zero velocity in the center of these recirculations. The velocity fluctuations on
597 the flow surface in the Right street are not observed in the depth-averaged velocity field.

598 The differences between the depth-averaged flow patterns and the surface flow patterns from
599 the 3D model are rather small, with the horizontal flow structures for the tested cases being
600 similar at different locations along the vertical direction, which favors the plausibility of
601 implementing depth-averaged 2D models to predict general flow patterns in urban areas.
602 However, in the areas with the presence of flow jet, the surface velocity is generally higher than
603 the depth-averaged velocity, this is consistent with findings of Li et al. (2024). Combined with
604 previous analysis of the significant vertical flow velocities inside flow jets, the limitations of
605 the 2D model to predict the flow jets in relatively large open areas are highlighted, which show
606 the additional merits of the 3D model when simulating complex urban floods.

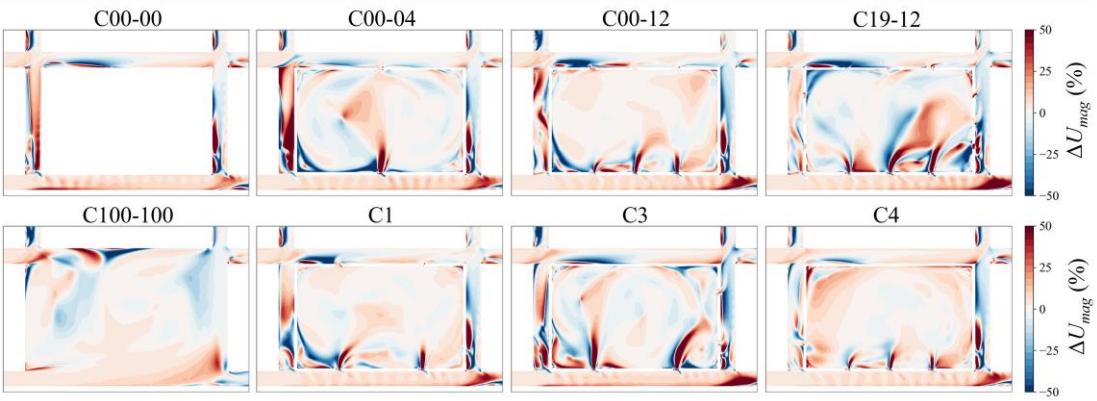

Figure 14 Contour plots of the differences between the surface velocity and the depth-averaged velocity ($U_{S,3D}$ -$U_{D,3D}$), locally normalized by the depth-averaged velocity.

4.3 Limitations and research needs

The current study selected eight representative configurations from the experimental data for in-depth analysis. The findings of this research provide valuable guidance for the detailed simulation of urban flooding, particularly in scenarios involving flow exchanges between flooded streets and the interior of buildings, a topic that is relatively rare in existing studies (Choley et al., 2021; Viccione et al., 2022). However, the configurations considered here may not be fully representative of more complex real-world urban areas (Dottori et al., 2013). Therefore, this study can be complemented with the analysis of real-word urban flood data and 3D simulations of more realistic configurations in order to reach a general conclusion. Further investigation is required to explore additional processes that were not addressed by the configurations tested in this study. This includes the influence of topographic effects, such as street width, steeper terrain slopes possibly leading to supercritical flow, and other geometric features typical of urbanized floodplains such as sidewalks (e.g., Bazin et al. (2017)) and uneven bottom elevation in open spaces.

In the current experiment, a fixed inflow rate was assumed, and overflow weirs were set to control the water level. This scenario simulated a situation in urban flooding where the flood source has a prolonged stable flow, resulting in a steady water level in the urban flooded area. In real-world flood scenarios, the flow rate of the flood source is often unsteady, varying over time due to factors such as rainfall intensity, catchment response, and upstream hydrological conditions. These time-varying inflow rates significantly influence urban flooding dynamics,

including water level fluctuations, flow velocities, and inundation patterns. Future research should prioritize incorporating more realistic flood scenarios, such as unsteady inflow conditions, to better understand their impacts on urban flooding. Studies like Mejía-Morales et al. (2023) have demonstrated the importance of considering unsteady inflow conditions in flood modelling, providing a valuable foundation for further exploration in this area.

The PVC and plastic materials used in the laboratory experiments cannot replicate the frictional forces present in real scenarios. The 3D simulations considered that the bed was hydraulically smooth. While the simulations replicate the laboratory conditions, they overlook the impact of friction in hydraulically rough beds, which needs to be considered in practical applications and future research.

The modelling assumptions, as outlined above, present potential challenges in practical applications. The high resource requirements for conducting field measurements and the representativeness and preciseness of the acquired data for model validation impose difficulties in applying numerical models to urban flood in actual urban settings, which is a central issue in the current research field (Costabile et al., 2020). Additionally, the application of 3D CFD models in large-scale urban flooding studies is significantly constrained by computational resources and efficiency. High computational costs, long simulation times, and the need for extensive memory and processing power are among the most critical challenges, often limiting the spatial and temporal resolution of such models (Afzal et al., 2017). These constraints not only affect the feasibility of large-scale simulations but also pose challenges in achieving a balance between model accuracy and computational practicality. Addressing these limitations requires advancements in computational hardware, efficient algorithms, and parallel computing techniques, which remain active areas of research in the field.

In the current study of urban flood intrusion into buildings and their interactions, only one scale of the scale-down model was selected. In related research, some researchers have conducted studies and discussions on different distortions in such scale-down models (Li et al., 2020). Such considerations hold significant value for understanding urban floods and applying

numerical simulation models. Therefore, further research in this area needs to be emphasized in future in-depth investigations.

With the development of high-performance computing, issues related to computational power will be partially resolved. Alternatively, applying different grid densities in the study area to reduce the total number of computational cells can also decrease the computing power demand (Zhang et al., 2018). Zhang et al. (2021) conducted an analysis on the sensitivity of the horizontal and vertical grids in a 3D hydrodynamic model, and the results showed that the horizontal grid has a greater impact on the outcomes than the vertical grid. Therefore, with improvements in computational power and performance, similar studies can provide valuable guidance for addressing this issue. With the further development of urban modelling, the integration of 3D hydrodynamic models with urban modelling will also be a key research direction for establishing a more comprehensive urban flood management system in the future (Elfouly et al., 2020; Jung Ok et al., 2021).

Furthermore, hydrodynamic model research and applications involve multi-dimensional coupling-related topics, such as coupling between 1D models of drainage systems and 2D or 3D models (Hu et al., 2023; Li et al., 2023; Seyoum Solomon et al., 2012). The measurement and calibration of hydraulic parameters involved (e.g., head loss coefficient) are also potential difficulties that hydrodynamic models may encounter in practical applications (Dottori et al., 2013; Rubinato, 2015). Additional topics of interest include unsteady flooding scenarios (El Kadi Abderrezzak et al., 2009; Mejía-Morales et al., 2023), and flow exchanges between the streets and the urban drainage system (Chang et al., 2018; Hossain Anni et al., 2020; Kitsikoudis et al., 2021; Martins et al., 2018; Rubinato et al., 2018).

5 Conclusion

Understanding the complex flow patterns in urban districts is of vital importance for improving the prediction accuracy of numerical tools. The current study focused on urban floods with flow intrusion into buildings and compared flow depths, partitioning of outflow discharges, and velocity fields computed with 2D and 3D numerical models against experimental observations

in a scaled model of a part of a street network in urban areas. Eight such urban configurations were considered with differences in the number and locations of the openings in the perimeter of the urban block that allow flow exchanges between the flooded streets and the interior of the block.

Both the 2D and 3D models predicted well the flow depth distribution in the streets and inside the porous blocks, with water depths gradually increasing within the block from the upstream to the downstream areas. The observed fluctuations of the flow surface along one of the streets were fairly well reproduced by the 3D model, which highlights the capacity of the applied 3D model to accurately capture the flow depths.

The partition of flow discharge at the street outlets is well reproduced by the 2D and 3D models for most cases (except C100-100), but the performance of the 3D model is superior to that of the 2D model, with the RMSEs in all tested cases being lower than1 pp for the 3D model, and between 1 and 2 pp for the 2D model.

The large flow surface recirculations are well reproduced by the 3D model regarding the number, locations and flow directionality, only with limited discrepancies in the size and shape for some cases. Flow intrusion into the porous urban blocks is more prominent through the openings along the streets with relatively high flow velocity. The predicted direction of the flow jet and the small recirculations match better the experimental observations when computed with the 3D model than when simulated with the 2D model of Dewals et al. (2023). These outcomes show the improved capacity of the 3D model for predicting flow patterns. The flow patterns of the depth-averaged velocity computed by the 3D model are very similar to the measured surface velocity fields.

The outcomes of the 3D computational modelling could also be useful for advancing the understanding of other effects of urban flooding, such as assessing the stability of pedestrians, vehicles, or urban furniture, modelling transport and mixing of contaminants or floating debris, or modelling flood damage and monetary losses. For instance, the current focus on flood entering buildings could be expanded to more diverse configurations, and urban models could

incorporate varying building distributions and surface types. In future research, with more extensive data and technological support, studies applying 3D hydrodynamic models should encompass a wider and more comprehensive range of scenarios to enhance their practical application. Based on the current research results, when simulating more urban flood scenarios in the future, the trade-off between different models should be fully considered. For example, the trade-off between the 2D model, which has the advantage of faster simulation speed, and the 3D model, which is slower in terms of computation but more accurate in current study scenarios.

Acknowledgements

This work was funded by the National Natural Science Foundation of China (No. 52309015), Guangxi Specific Research Project for Research Bases and Talents (No. AD23026176), Guangxi Science and Technology Major Project (No. AA23023009), the Natural Science Foundation of Guangdong Province (No. 2023B1515020087). The support from the French National Research Agency (ANR) for the project DEUFI (ANR-18-CE01-0020) is also acknowledged.

Supplemental data

Supporting Information related to this article is available, including figures and tables.

References

Arrault, A., Finaud-Guyot, P., Archambeau, P., Bruwier, M., Erpicum, S., Pirotton, M., & Dewals, B., 2016. Hydrodynamics of long-duration urban floods: experiments and numerical modelling. Natural Hazards and Earth System Sciences, 16(6): 1413-1429. DOI:10.5194/nhess-16-1413-2016

Bazin, P.-H., Mignot, E., & Paquier, A., 2017. Computing flooding of crossroads with obstacles using a 2D numerical model. Journal of Hydraulic Research, 55(1): 72-84. DOI:10.1080/00221686.2016.1217947

Bruwier, M., Maravat, C., Mustafa, A., Teller, J., Pirotton, M., Erpicum, S., . . . Dewals, B., 2020. Influence of urban forms on surface flow in urban pluvial flooding. Journal of Hydrology, 582: 124493. DOI:https://doi.org/10.1016/j.jhydrol.2019.124493

Chang, T.-J., Wang, C.-H., Chen, A. S., & Djordjević, S., 2018. The effect of inclusion of inlets in dual drainage modelling. Journal of Hydrology, 559: 541-555. DOI:https://doi.org/10.1016/j.jhydrol.2018.01.066

Chanson, H., 2004. Hydraulics of open channel flow. Elsevier.

Chen, W., Wang, W., Mei, C., Chen, Y., Zhang, P., & Cong, P., 2024. Multi-objective decision-making for green infrastructure planning: Impacts of rainfall characteristics and infrastructure configuration. Journal of Hydrology, 628: 130572. DOI:https://doi.org/10.1016/j.jhydrol.2023.130572

Chen, X., Zhu, D. Z., & Steffler, P. M., 2017. Secondary currents induced mixing at channel confluences. Canadian Journal of Civil Engineering, 44(12): 1071-1083. DOI:10.1139/cjce-2016-0228

Chen, Y., Zhou, H., Zhang, H., Du, G., & Zhou, J., 2015. Urban flood risk warning under rapid urbanization. Environmental Research, 139: 3-10. DOI:https://doi.org/10.1016/j.envres.2015.02.028

Choley, C., Finaud-Guyot, P., Garambois, P.-A., & Mose, R. (2021). An effective urban flood model accounting for street-building exchanges. Paper presented at the SimHydro 21: Models for complex and global water issues–Practices & expectations.

Costabile, P., Costanzo, C., De Lorenzo, G., & Macchione, F., 2020. Is local flood hazard assessment in urban areas significantly influenced by the physical complexity of the hydrodynamic inundation model? Journal of Hydrology, 580: 124231. DOI:https://doi.org/10.1016/j.jhydrol.2019.124231

Deng, Z., Wu, X., Villarini, G., Wang, Z., Zeng, Z., & Lai, C., 2024. Stronger exacerbation of extreme rainfall at the hourly than daily scale by urbanization in a warming climate. Journal of Hydrology, 633: 131025. DOI:https://doi.org/10.1016/j.jhydrol.2024.131025

Dewals, B., Kitsikoudis, V., Mejía-Morales, M. A., Archambeau, P., Mignot, E., Proust, S., . . . Paquier, A., 2023. Can the 2D shallow water equations model flow intrusion into buildings during urban floods? Journal of Hydrology, 619: 129231. DOI:https://doi.org/10.1016/j.jhydrol.2023.129231

Dong, B., Xia, J., Zhou, M., Deng, S., Ahmadian, R., & Falconer, R. A., 2021. Experimental and numerical model studies on flash flood inundation processes over a typical urban street. Advances in Water Resources, 147: 103824. DOI:https://doi.org/10.1016/j.advwatres.2020.103824

Dottori, F., Di Baldassarre, G., & Todini, E., 2013. Detailed data is welcome, but with a pinch of salt: Accuracy, precision, and uncertainty in flood inundation modeling. Water Resources Research, 49(9): 6079–6085-6079–6085.

Dottori, F., & Todini, E., 2013. Testing a simple 2D hydraulic model in an urban flood experiment. Hydrological Processes, 27(9): 1301-1320. DOI:https://doi.org/10.1002/hyp.9370

El Kadi Abderrezzak, K., Lewicki, L., Paquier, A., Rivière, N., & Travin, G., 2011. Division of critical flow at three-branch open-channel intersection. Journal of Hydraulic Research, 49(2): 231-238.

El Kadi Abderrezzak, K., Paquier, A., & Mignot, E., 2009. Modelling flash flood propagation in urban areas using a two-dimensional numerical model. Natural Hazards, 50(3): 433–460-433–460.

Elfouly, M., & Labetski, A., 2020. Flood damage cost estimation in 3D based on an indicator modelling framework. Geomatics, Natural Hazards and Risk, 11(1): 1129-1153. DOI:10.1080/19475705.2020.1777213

Fang, Q., 2016. Adapting Chinese cities to climate change. Science, 354(6311): 425-426. DOI:10.1126/science.aak9826

789 Finaud-Guyot, P., Garambois, P. A., Araud, Q., Lawniczak, F., François, P., Vazquez, J., &
790 Mosé, R., 2018. Experimental insight for flood flow repartition in urban areas. Urban
791 Water Journal, 15(3): 242-250. DOI:10.1080/1573062X.2018.1433861

792 Finaud-Guyot, P., Garambois, P. A., Dellinger, G., Lawniczak, F., & François, P., 2019.
793 Experimental characterization of various scale hydraulic signatures in a flooded
794 branched street network. Urban Water Journal, 16(9): 609-624.

795 Fujita, I., Muste, M., & Kruger, A., 1998. Large-scale particle image velocimetry for flow
796 analysis in hydraulic engineering applications. Journal of Hydraulic Research, 36(3):
797 397-414.

798 Güney, M. S., Tayfur, G., Bombar, G., & Elci, S., 2014. Distorted Physical Model to Study
799 Sudden Partial Dam Break Flows in an Urban Area. Journal of Hydraulic Engineering,
800 140(11): 05014006. DOI:10.1061/(ASCE)HY.1943-7900.0000926

801 Guo, K. H., Guan, M. F., & Yu, D. P., 2021. Urban surface water flood modelling - a
802 comprehensive review of current models and future challenges. Hydrology and Earth
803 System Sciences, 25(5): 2843-2860. DOI:10.5194/hess-25-2843-2021

804 Hettiarachchi, S., Wasko, C., & Sharma, A., 2018. Increase in flood risk resulting from climate
805 change in a developed urban watershed – the role of storm temporal patterns.
806 Hydrology and Earth System Sciences, 22(3): 2041-2056. DOI:10.5194/hess-22-2041-
807 2018

808 Hirt, C. W., & Nichols, B. D., 1981. Volume of fluid (VOF) method for the dynamics of free
809 boundaries. Journal of Computational Physics, 39(1): 201-225.
810 DOI:https://doi.org/10.1016/0021-9991(81)90145-5

811 Hossain Anni, A., Cohen, S., & Praskievicz, S., 2020. Sensitivity of urban flood simulations to
812 stormwater infrastructure and soil infiltration. Journal of Hydrology, 588: 125028.
813 DOI:https://doi.org/10.1016/j.jhydrol.2020.125028

814 Hu, G., Zou, L., O'Grady, D. J., & Hu, R., 2023. An integrated coupling model for solving
815 multiscale fluid-fluid coupling problems in SAM code. Nuclear Engineering and
816 Design, 404: 112186. DOI:https://doi.org/10.1016/j.nucengdes.2023.112186

817 Jung Ok, K., & Jae Kang, L., 2021. Urban Flood Inundation Simulation Based on High-
818 Precision 3D Modeling. Journal of Coastal Research, 114(sp1): 454-458.
819 DOI:10.2112/JCR-SI114-092.1

820 Kitsikoudis, V., Erpicum, S., Rubinato, M., Shucksmith, J. D., Archambeau, P., Pirotton, M.,
821 & Dewals, B., 2021. Exchange between drainage systems and surface flows during
822 urban flooding: Quasi-steady and dynamic modelling in unsteady flow conditions.
823 Journal of Hydrology, 602: 126628.
824 DOI:https://doi.org/10.1016/j.jhydrol.2021.126628

825 Kreibich, H., Thaler, T., Glade, T., & Molinari, D., 2019. Preface: Damage of natural hazards:
826 assessment and mitigation. Natural Hazards and Earth System Sciences, 19(3): 551–
827 554.

828 Lai, C., Luo, Y., Li, X., Yu, H., Zeng, Z., Li, S., . . . Wang, Z., 2024. Assessment on
829 vulnerability of road networks considering the dynamic impact of urban waterlogging
830 and the mitigation effect of LID measures. Journal of Hydrology, 643: 132005.
831 DOI:https://doi.org/10.1016/j.jhydrol.2024.132005

832 Li, C., Sun, N., Lu, Y., Guo, B., Wang, Y., Sun, X., & Yao, Y. (2023). Review on Urban Flood
833 Risk Assessment. Sustainability, 15(1). doi:10.3390/su15010765

834 Li, S., Wang, Z., Lai, C., & Lin, G., 2020. Quantitative assessment of the relative impacts of
835 climate change and human activity on flood susceptibility based on a cloud model.
836 Journal of Hydrology, 588: 125051.

Li, X., Dellinger, G., Erpicum, S., Chen, L., Yu, S., Guiot, L., . . . Dewals, B., 2024. 2D and 3D Computational Modeling of Surface Flooding in Urbanized Floodplains: Modeling Performance for Various Building Layouts. WATER RESOURCES RESEARCH, 60(5): e2023WR035149. DOI:https://doi.org/10.1029/2023WR035149

Li, X., Erpicum, S., Bruwier, M., Mignot, E., Finaud-Guyot, P., Archambeau, P., . . . Dewals, B., 2019. Technical note: Laboratory modelling of urban flooding: strengths and challenges of distorted scale models. Hydrology and Earth System Sciences, 23(3): 1567-1580. DOI:10.5194/hess-23-1567-2019

Li, X., Erpicum, S., Mignot, E., Archambeau, P., Pirotton, M., & Dewals, B., 2021. Influence of urban forms on long-duration urban flooding: Laboratory experiments and computational analysis. Journal of Hydrology, 603: 127034. DOI:https://doi.org/10.1016/j.jhydrol.2021.127034

Li, X., Erpicum, S., Mignot, E., Archambeau, P., Pirotton, M., & Dewals, B., 2022. Laboratory modelling of urban flooding. Scientific Data, 9(1): 159. DOI:10.1038/s41597-022-01282-w

Li, X., Erpicum, S., Mignot, E., Archambeau, P., Rivière, N., Pirotton, M., & Dewals, B., 2020. Numerical insights into the effects of model geometric distortion in laboratory experiments of urban flooding. Water Resources Research, 56(7): e2019WR026774.

Li, X., Kitsikoudis, V., Mignot, E., Archambeau, P., Pirotton, M., Dewals, B., & Erpicum, S., 2021. Experimental and Numerical Study of the Effect of Model Geometric Distortion on Laboratory Modeling of Urban Flooding. Water Resources Research, 57(10): e2021WR029666. DOI:https://doi.org/10.1029/2021WR029666

Liao, Y., Wang, Z., Chen, X., & Lai, C., 2023. Fast simulation and prediction of urban pluvial floods using a deep convolutional neural network model. Journal of Hydrology, 624: 129945. DOI:https://doi.org/10.1016/j.jhydrol.2023.129945

Luo, H., Fytanidis, D. K., Schmidt, A. R., & García, M. H., 2018. Comparative 1D and 3D numerical investigation of open-channel junction flows and energy losses. Advances in Water Resources, 117: 120-139. DOI:https://doi.org/10.1016/j.advwatres.2018.05.012

Luo, P., Luo, M., Li, F., Qi, X., Huo, A., Wang, Z., . . . Wang, Y., 2022. Urban flood numerical simulation: Research, methods and future perspectives. Environmental Modelling & Software, 156: 105478. DOI:https://doi.org/10.1016/j.envsoft.2022.105478

Martins, R., Rubinato, M., Kesserwani, G., Leandro, J., Djordjevic, S., & Shucksmith, J. D., 2018. On the Characteristics of Velocities Fields in the Vicinity of Manhole Inlet Grates During Flood Events. Water Resources Research, 54(9): 6408-6422.

Mejía-Morales, M. A., Mignot, E., Paquier, A., & Proust, S. 2022. Dataset of a laboratory experiment on the effect of the storage capacity of a city block on unsteady urban floodwaters [Dataset]. DOI:https://doi.org/10.57745/BFHGO3

Mejía-Morales, M. A., Mignot, E., Paquier, A., & Proust, S., 2023. Laboratory Investigation Into the Effect of the Storage Capacity of a City Block on Unsteady Urban Flood Flows. WATER RESOURCES RESEARCH, 59(4): e2022WR032984. DOI:https://doi.org/10.1029/2022WR032984

Mejía-Morales, M. A., Mignot, E., Paquier, A., Sigaud, D., & Proust, S., 2021. Impact of the porosity of an urban block on the flood risk assessment: A laboratory experiment. Journal of Hydrology, 602: 126715. DOI:https://doi.org/10.1016/j.jhydrol.2021.126715

Mejía Morales, M. A., 2022. Influence of the flow exchanges between streets and a city block during urban floods : Laboratory experiments under steady and unsteady flow conditions. Ph. D. Thesis, Université de Lyon.

Mignot, E., Bonakdari, H., Knothe, P., Kouyi, G. L., Bessette, A., Riviere, N., & Bertrand-Krajewski, J. L., 2012. Experiments and 3D simulations of flow structures in junctions and their influence on location of flowmeters. Water Science and Technology, 66(6): 1325-1332. DOI:10.2166/wst.2012.319

Mignot, E., & Dewals, B., 2022. Hydraulic modelling of inland urban flooding: Recent advances. Journal of Hydrology, 609: 127763. DOI:https://doi.org/10.1016/j.jhydrol.2022.127763

Mignot, E., Li, X., & Dewals, B., 2019. Experimental modelling of urban flooding: A review. Journal of Hydrology, 568: 334-342. DOI:https://doi.org/10.1016/j.jhydrol.2018.11.001

Mignot, E., Zeng, C., Dominguez, G., Li, C. W., Rivière, N., & Bazin, P. H., 2013. Impact of topographic obstacles on the discharge distribution in open-channel bifurcations. Journal of Hydrology, 494: 10-19.

Momplot, A., Kouyi, G. L., Mignot, E., Rivière, N., & Bertrand-Krajewski, J.-L., 2017. Typology of the flow structures in dividing open channel flows. Journal of Hydraulic Research, 55(1): 63-71.

Mu, Y., Li, Y., Yan, R., Luo, P. P., Liu, Z., Sun, Y. Y., . . . Zha, X. B., 2024. Analysis of the Ongoing Effects of Disasters in Urbanization Process and Climate Change: China's Floods and Droughts. Sustainability, 16(1). DOI:10.3390/su16010014

Paquier, A., Mangara, C., Mignot, E., Li, X., & Dewals, B. (2022, 2022//). 2-D Simulation of Flow Entering a Building. Paper presented at the Advances in Hydroinformatics, Singapore.

Ramamurthy, A. S., Qu, J., & Vo, D., 2007. Numerical and Experimental Study of Dividing Open-Channel Flows. Journal of Hydraulic Engineering, 133(10): 1135-1144. DOI:10.1061/(ASCE)0733-9429(2007)133:10(1135)

Reduction, U. O. f. D. R. (2020). The Human Cost of Disasters: An Overview of the Last 20 Years (2000–2019). In: UN Office for Disaster Risk Reduction Geneva, Switzerland.

Rong, Y., Zhang, T., Zheng, Y., Hu, C., Peng, L., & Feng, P., 2020. Three-dimensional urban flood inundation simulation based on digital aerial photogrammetry. Journal of Hydrology, 584: 124308. DOI:https://doi.org/10.1016/j.jhydrol.2019.124308

Rosenzweig, B. R., Herreros Cantis, P., Kim, Y., Cohn, A., Grove, K., Brock, J., . . . Chang, H., 2021. The Value of Urban Flood Modeling. Earth's Future, 9(1): e2020EF001739. DOI:https://doi.org/10.1029/2020EF001739

Rubinato, M., 2015. Physical Scale Modelling of Urban Flood Systems. Ph.D. Thesis, University of Sheffield.

Rubinato, M., Helms, L., Vanderlinden, M., Hart, J., & Martins, R., 2022. Flow exchange, energy losses and pollutant transport in a surcharging manhole linked to street profiles. Journal of Hydrology, 604: 127201. DOI:https://doi.org/10.1016/j.jhydrol.2021.127201

Rubinato, M., Lee, S., Martins, R., & Shucksmith, J. D., 2018. Surface to sewer flow exchange through circular inlets during urban flood conditions. Journal of Hydroinformatics, 20(3): 564-576.

Schindfessel, L., Creëlle, S., & De Mulder, T., 2015. Flow Patterns in an Open Channel Confluence with Increasingly Dominant Tributary Inflow. Water, 7(9): 4724–4751-4724–4751.

Seyoum Solomon, D., Vojinovic, Z., Price Roland, K., & Weesakul, S., 2012. Coupled 1D and Noninertia 2D Flood Inundation Model for Simulation of Urban Flooding. Journal of Hydraulic Engineering, 138(1): 23-34. DOI:10.1061/(ASCE)HY.1943-7900.0000485

Smith, G. P., Rahman, P. F., & Wasko, C., 2016. A comprehensive urban floodplain dataset for model benchmarking. International Journal of River Basin Management, 14(3): 345-356. DOI:10.1080/15715124.2016.1193510

Sturm, M., Gems, B., Keller, F., Mazzorana, B., Fuchs, S., Papathoma-Köhle, M., & Aufleger, M., 2018. Experimental analyses of impact forces on buildings exposed to fluvial hazards. Journal of Hydrology, 565: 1-13. DOI:https://doi.org/10.1016/j.jhydrol.2018.07.070

Torres, C., Borman, D., Matos, J., & Neeve, D., 2022. CFD modeling of scale effects on free-surface flow over a labyrinth weir and spillway. Journal of Hydraulic Engineering, 148(7): 04022011. DOI:10.1061/(ASCE)HY.1943-7900.0001989

Velickovic, M., Zech, Y., & Soares-Frazão, S., 2017. Steady-flow experiments in urban areas and anisotropic porosity model. Journal of Hydraulic Research, 55(1): 85-100. DOI:10.1080/00221686.2016.1238013

Versteeg, H. K., Malalasekera, W., 2007. An Introduction to Computational Fluid Mechanics: The Finite Volume Method. Pearson.

Viccione, G., & Izzo, C., 2022. Three-dimensional CFD modelling of urban flood forces on buildings: a case study. Journal of Physics: Conference Series, 2162(1): 012020. DOI:10.1088/1742-6596/2162/1/012020

Weber, L. J., Schumate, E. D., & Mawer, N., 2001. Experiments on flow at a 90° open-channel junction. Journal of Hydraulic Engineering, 127(5): 340-350.

Xia, J., Falconer, R. A., Wang, Y., & Xiao, X., 2014. New criterion for the stability of a human body in floodwaters. Journal of Hydraulic Research, 52(1): 93-104.

Yang, W., Xu, K., Lian, J., Bin, L., & Ma, C., 2018. Multiple flood vulnerability assessment approach based on fuzzy comprehensive evaluation method and coordinated development degree model. Journal of Environmental Management, 213: 440-450. DOI:https://doi.org/10.1016/j.jenvman.2018.02.085

Zhang, B., Wu, B., Zhang, R., Ren, S., & Li, M., 2021. 3D numerical modelling of asynchronous propagation characteristics of flood and sediment peaks in three gorges reservoir. Journal of Hydrology, 593: 125896. DOI:https://doi.org/10.1016/j.jhydrol.2020.125896

Zhang, T., Peng, L., & Feng, P., 2018. Evaluation of a 3D unstructured-mesh finite element model for dam-break floods. Computers & Fluids, 160: 64-77. DOI:https://doi.org/10.1016/j.compfluid.2017.10.013

Zhou, Q., Yu, W., Chen, A., Jiang, C., Fu, G., Savic, D., & Djordjevic, S., 2016. Laboratory analysis of Building blockage effects on urban flood propagation.

Zhou, Q. Y., Wangyang; Chen, Albert S.; Jiang, Chunbo; Fu, Guangtao; Savić, Dragan A.; Djordjević, Slobodan, 2016. Laboratory Analysis of Building Blockage Effects on Urban Flood Propagation. Vodoprivreda, 48(282-284): 147-154.

Zhu, Z., Gou, L., Liu, S., & Peng, D., 2023. Effect of urban neighbourhood layout on the flood intrusion rate of residential buildings and associated risk for pedestrians. Sustainable Cities and Society, 92: 104485. DOI:https://doi.org/10.1016/j.scs.2023.104485

Declaration of interests

☒The authors declare that they have no known competing financial interests or personal relationships that could have appeared to influence the work reported in this paper.

☐The authors declare the following financial interests/personal relationships which may be considered as potential competing interests: